ChemComm

ROYAL SOCIETY OF CHEMISTRY

FEATURE ARTICLE

View Article Online
View Journal | View Issue



Cite this: *Chem. Commun.*, 2026, **62**, 5141

# Transition metal dichalcogenide catalysts incorporating hollow carbon spheres toward water splitting and supercapacitors

Xiao Zhang *

Transition metal dichalcogenides (TMDs), *e.g.*, $MoS_2$ and $MoSe_2$, are widely used as catalysts for electrochemical water splitting and green energy conversion because of their high stability and favorable hydrogen adsorption energies. However, their intrinsically low electrical conductivity and limited surface area often lead to poor hydrogen evolution reaction (HER) performance. The high conductivity and layered structure of hollow carbon spheres (HCSs) compensate for these shortcomings, thus combining TMDs with HCSs has been extensively investigated. In addition, non-metal dopants can be introduced into carbon frameworks to control the growth of hybrid TMD nanostructures and to increase electrochemical activity by creating additional active sites. This review first focuses on the development of N-, O-, and P-doped HCSs, reviewing synthesis routes, layer numbers, and performance metrics. It then highlights recent advances in integrating layered molybdenum sulfide and selenide with HCSs, emphasizing synthesis methods, composition tuning, heterojunction formation, as well as electrochemical applications such as water splitting and supercapacitors, while systematically discussing growth kinetics and the influence of Ni and Co based components. Finally, the article addresses the remaining challenges and outlines future prospects for TMD–HCS composite catalysts in advanced applications.

Received 27th December 2025,
Accepted 2nd February 2026

DOI: 10.1039/d5cc07364b

rsc.li/chemcomm



## Introduction

The development of green energy conversion technologies has attracted significant attention as a promising alternative to traditional fossil fuels.[1–3] Because of its high energy density and carbon-free nature, hydrogen ($H_2$) is widely regarded as a leading clean energy carrier.[4,5] Green hydrogen produced *via* electrochemical water splitting has been widely developed as a leading technology in emerging energy sectors.[6–8] During water splitting, the hydrogen evolution reaction (HER) occurs at the cathode while the oxygen evolution reaction (OER) occurs at the anode, driving the operation of water electrolyzers.[9,10] The efficiency of catalysts plays an important role in this case, and environmentally friendly energy storage technologies are urgently needed to support the advancement of artificial intelligence (AI) and big data.[11–13] Supercapacitors, promising for AI applications, are attracting significant attention because of their high power density and rapid charge–discharge capability.[14–17] These studies have focused on improving energy density and cyclic stability, both of which depend strongly on catalyst performance.

Layered two-dimensional (2D) transition metal dichalcogenides (TMDs) are investigated as bifunctional electrocatalysts for overall water splitting because their stacked structures provide efficient charge-transport pathways and large specific surface areas.[18–26] The catalytic performance of TMDs is highly sensitive to chemical and phase composition, size distribution, and microstructure. For example, molybdenum disulfide ($MoS_2$) has been extensively studied for the HER due to its

*Advanced Institute for Materials Research (WPI-AIMR), Tohoku University, Sendai, 980-8577, Japan. E-mail: zhang.xiao.d8@tohoku.ac.jp*

**Xiao Zhang**

*Xiao Zhang obtained her Honours Bachelor of Science degree from University of Toronto (Canada) and Master of Philosophy degree from University of New South Wales (Australia). She was awarded with Doctor of Philosophy by Curtin University (Australia). Her research interests encompass carbon-based materials, carbon dioxide conversion, water splitting, photo-/electrochemical catalysis, and luminescent materials. Xiao Zhang worked at Cracow University of Technology before she joined Advanced Institute for Materials Research at Tohoku University as an associate professor in 2025.*

high stability, a near-optimal hydrogen adsorption free energy $\Delta G_H^*$ = 0.08 eV, and comparable d-band electronic and chemical properties.[27,28] However, the HER activity of $MoS_2$ is generally poorer in alkaline media than in acidic solvents. The OER performance of $MoS_2$ is also strongly influenced by its edge sites. Moreover, the impact of phase composition on TMD electrochemical behaviour, such as the 1T and 2H phases of $MoS_2$, has attracted considerable attention. Because a single type of TMDs could rarely serve as an effective bifunctional catalyst, current research emphasizes controlling synthesis kinetics to increase active site density, suppress aggregation, tune composition, construct heterostructures for favourable band alignment, and enhance conductivity. To overcome intrinsic limitations, these 2D TMDs are often integrated with other layered materials, including hollow carbon, graphene, and MXene.[29–32]

Carbon-based nanomaterials, such as graphene, carbon nanotubes, and hollow carbon spheres (HCSs), provide effective support for TMD electrocatalysts by enhancing conductivity, increasing the number of active sites, and preventing nanosheet aggregation.[13–16] HCSs are particularly advantageous because their hollow structures relieve mechanical stress and prevent structural collapse of active materials during electrode operation, thereby improving cyclic stability. A variety of hollow carbon structures have been synthesized using different strategies. For example, Wei and co-workers reported a yolk–shell porous carbon sphere as an electrode material for high-performance capacitive deionization.[33] Liao *et al.* prepared novel flower-like hierarchical carbon spheres featuring multi-scale pores,[34] while Huang *et al.* reported a kinetics-controlled, ultrafast co-assembly strategy to construct hollow mesoporous carbon spheres for high-performance supercapacitors.[11] Single and multilayer HCSs have been created through various chemical approaches, most notably the hard template method. In contrast to soft template approaches, hard template methods using materials such as metal oxides, polymer spheres, or inorganic salts, are widely employed for the fabrication of hollow carbon structures due to their superior controllability. The preparation process including the template removal step critically influence the microstructures, wall thicknesses, and overall activities of the HCSs. Among the template choices, silica ($SiO_2$) spheres of different sizes have attracted the greatest attention due to their easy availability and controllability *via* the classical Stöber method.[35] During synthesis, a polymerization reaction between soluble phenolic resin (PR) and formaldehyde occurs on the surface of the $SiO_2$ spheres, yielding hollow PR spheres. These can then be converted into HCSs by removing the $SiO_2$ with a NaOH solution. By carefully controlling the deposition of $SiO_2$ gel and organic layers, the number of HCS layers has been tuned from one up to seven, as reported in the literature.[36] Single and double layered HCSs have been extensively investigated for energy conversion applications. Single-shelled HCSs exhibit thin carbon shells and a high density of accessible active sites, which facilitates controlled growth of TMDs on their surfaces. However, their structural stability is often insufficient, particularly in supercapacitor systems, due to limited mechanical robustness and suboptimal space utilization. In contrast, double-shelled HCSs offer significantly enhanced structural stability and improved space utilization, making them more suitable for applications requiring long-term cyclic durability.

Hollow carbon electrodes have been extensively investigated as supercapacitor materials due to their chemical inertness, excellent electrical conductivity, long-term cyclic stability, and large internal void space. To enhance the energy density of double-layer supercapacitors, porous carbon nanomaterials doped with non-metal elements (such as N, O, B, and P) have been developed.[15,37,38] These heteroatoms are incorporated into the carbon framework to increase the specific surface area, generate hierarchical porous structures that facilitate electrolyte transport and ion exchange, and introduce redox active sites that contribute pseudocapacitance through faradaic reactions. For instance, Yang's group reported N- and O-doped HCSs with mesoporous structures, achieving a specific surface area as high as 935 $m^2\ g^{-1}$.[38] The well-defined porous structure significantly improved ion and electron transport, while the high heteroatom content ($\sim$30%) provided substantial pseudocapacitance *via* redox reactions of functional groups. In addition to non-metal doping, noble metals and transition metals have also been incorporated into hollow carbons to further enhance electrochemical performance.[39–43] Such metal-loaded hollow carbon nanomaterials have been developed for diverse applications in green energy conversion.

The integration of 2D TMDs with HCSs has been extensively investigated in the HER, OER, oxygen reduction reaction (ORR), batteries, supercapacitors, and other energy related applications. Among the TMDs, transition metal sulfides are widely studied.[36,44–46] The hexagonal arrangement of $MoS_2$ nanosheets provides abundant active sites and orbitals favorable for oxidative intermediates, thus enhancing the catalytic performance of the material. Furthermore, cobalt-doped 1T-$MoS_2$ heterogeneous interfaces optimize the Gibbs free energy of hydrogen adsorption ($\Delta G_H^*$) and reduce intermediate adsorption, resulting in improved HER activity.[46] Iron- and nickel-doped $MoS_2$ have also been reported as bifunctional electrocatalysts, simultaneously enhancing HER and OER performance.[45] In addition, hybrid $Co_9S_8$–$MoS_2$ alloys incorporated with HCSs effectively mitigate the capacity fading during cycling by stabilizing the $MoS_2$ nanosheet structure.[7] Layered selenides such as $MoSe_2$ and $NiSe_2$ have likewise been integrated with hollow carbon materials, due to the great potential of TMD-HCS composites as efficient bifunctional catalysts for diverse energy conversion and storage applications.[10,48–51] For example, Luan and co-workers demonstrated the growth of $MoS_{2-2x}Se_{2x}$ nanosheets on HCSs, achieving enhanced electrochemical performance.[50]

The synthesis kinetics of HCSs and their incorporation with TMDs present important challenges that warrant detailed mechanistic and application-oriented studies. Layered TMDs can grow both vertically and horizontally onto hollow carbon substrates.[13,52,53] For instance, $MoS_2$ nanosheets have been deposited either on the surfaces or within HCSs, exhibiting distinct electrochemical activities.[37] Kinetic control of $MoS_2$ growth on HCSs has revealed the complex interaction processes between

 

$MoS_2$ and carbon frameworks. Moreover, the strong interfacial bonding and uniform distribution of TMDs on HCSs play a critical role in determining the catalytic performance of the resulting composites. HCSs synthesized using $SiO_2$ templates are frequently employed for loading layered TMDs, as the reaction between silica and metal ions facilitates tight integration with the carbon matrix and ensures homogeneous distribution.[54] For example, Liu *et al.* fabricated shape-controlled cobalt–molybdenum silicate nanosheet arrays on HCSs, which were subsequently converted into $Co_9S_8$–$MoS_2$@HCS composites *via in situ* sulfurization using S ions in place of silicate ions.[7] These composites demonstrated superior electrochemical activity, enhanced specific capacity, and improved cyclic stability of the electrode material.

A large number of TMD-incorporated hollow carbon composites have been reported, demonstrating promising electrochemical activities. These composites have shown significant potential in green energy conversion, including applications in electrochemical water splitting for the HER and OER, electrochemical redox processes for chemical fuel production, and as electrode materials for batteries and supercapacitors. When layered TMD nanomaterials are integrated with HCSs, the charge carrier transport pathways are enhanced, increasing the density of active sites available for redox reactions. Despite these advances, relatively few reviews have addressed the synthesis control and energy conversion applications of TMD–HCS composites. Some of the published review articles have summarized the challenges associated with HCSs in advanced electrocatalytic applications; however, comprehensive coverage of their roles in energy conversion remains limited. Owing to their unique morphology and outstanding catalytic activity, HCSs have emerged as important materials in the field of energy chemistry.

This review emphasizes recent progress in TMD–HCS composite catalysts, focusing on key aspects such as synthesis control of single and multilayer HCSs, the influence of non-metal doping, the growth and compositional tuning of TMDs on HCSs, bandgap modulation, and overall catalytic performance. Our recent work has centred on the design and synthesis of hollow carbon nanostructures.[10,12,18,29,33] Through hard template strategies, we established synthetic routes for single- and multi-layered HCS-based nanoskeletons. Their performance was further enhanced through non-metal heteroatom doping. Moreover, a range of TMDs was incorporated either within the cavities or on the outer surfaces of these HCSs to probe their electrochemical properties. Recognizing the central role of HCSs in electrochemical systems, this review highlights recent progress in the synthesis and application of TMD/HCS-based catalysts. Fig. 1 shows an overview of the key aspects reviewed for TMD–HCS composite catalysts in green energy conversion. The discussion begins with synthesis control, which is fundamental to tailoring composite properties. Topics include synthetic regulation, non-metal doping (*e.g.*, N, O, and P), and the resulting electrochemical performance of HCSs. The growth of $MoS_2$ nanosheets is then examined, highlighting growth orientations (vertical or horizontal) and deposition positions

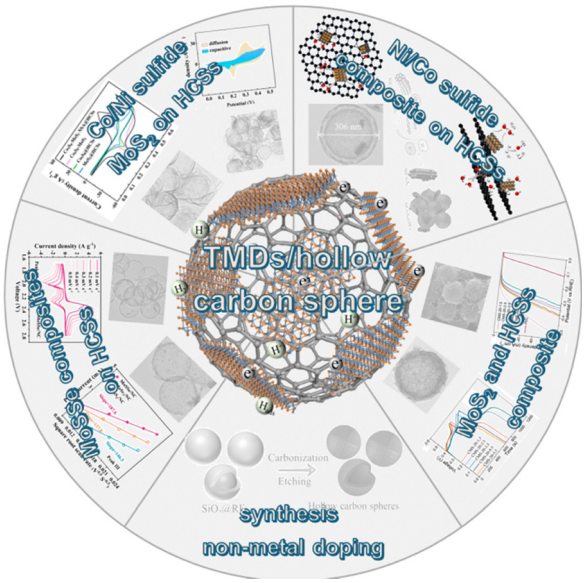


Fig. 1 Key aspects of TMD–HCS composite catalysts in the context of green energy conversion.

(inside or outside of HCSs). This review also covers the development of $MoSe_2$, $MoS_2/MoSe_2$ alloys, and other TMDs such as $NiS_2$, $NiS/Ni_3S_4$, and $NiCo_2S_4$. Practical applications of these composites represent another major focus, with emphasis on their roles in electrochemical processes, HER/OER performance, and supercapacitor applications. Finally, the review addresses the major challenges and future prospects of TMD-HCS composite catalysts in energy related technologies.

## Synthesis and non-metal doping of HCSs

Carbon electrodes, particularly hollow carbon-based materials such as 1D nanotubes, 2D graphene, and 3D HCSs, have played pivotal roles in green energy conversion systems, including batteries and supercapacitors, due to their excellent conductivity and long-term cyclic stability.[55,56] Among these, HCSs are especially advantageous due to their large internal voids, micrometre scale dimensions, and robust physicochemical stability.[57,58] Considerable progress has been made in both the synthesis and application of HCSs. The hard template method, one of the most widely adopted strategies, has been extensively developed for fabricating HCSs for energy storage and conversion.[59–62] This approach relies on templates that can be readily inserted and removed. Carbon precursors are often formed through the co-condensation of polymers and resins on the template surfaces. Subsequent high-temperature removal of the template yields the target carbon shells. Careful assembly and deposition of the precursors on the template were key to ensuring uniform cavity diameters and precise shell thicknesses.

Among the various hard templates, sol–gel $SiO_2$ spheres are frequently employed due to their inert nature, low cost, and ease of preparation and control. In early studies, the

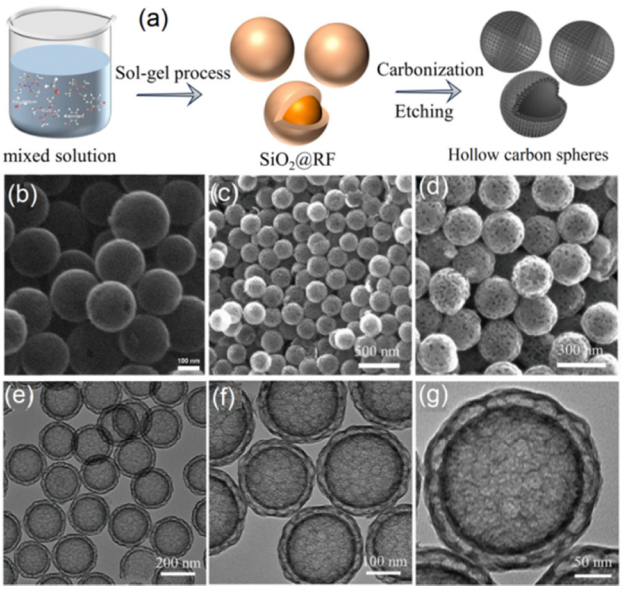


Fig. 2 (a) Schematic illustration of the typical preparation procedure of HCSs using $SiO_2$ templates. (b) SEM images obtained for an example of single-layer HCSs. (c) and (d) SEM images of double-layer HCSs. (e)–(g) TEM images of double-layer HCSs. (a) and (b) were reproduced with permission from ref. 64. Copyright 2025 Elsevier. (c)–(g) Were reproduced with permission from ref. 65. Copyright 2022 Wiley-VCH GmbH.

polymerization of soluble PR with formaldehyde was carried out on the surface of $SiO_2$ spheres, forming a carbon precursor layer. HCSs could be fabricated through subsequent high-temperature carbonization followed by removal of the $SiO_2$ cores with NaOH solution.[63,64] A quite common preparation process is illustrated in Fig. 2a.[65] In this approach, the sol–gel $SiO_2$ spheres synthesized *via* the classical Stöber method were dispersed in water, where resorcinol and formaldehyde polymerized to form a resorcinol-formaldehyde (RF) layer on the template surface. Single-layer HCSs were then obtained by carbonization at 700 °C followed by template removal using a NaOH solution, and uniform hollow spheres were successfully fabricated as shown in the SEM image in Fig. 2b. Moreover, the wall thicknesses of the HCSs can be tuned by adjusting the deposition time of the RF layers.

In the case of the $SiO_2$ template method developed for fabricating HCSs, the diameters and shell thicknesses of HCSs can be precisely tuned by adjusting the size of the $SiO_2$ spheres and the polymerization time. The intrinsic porous structure of sol–gel $SiO_2$ spheres imparts distinctive porosity to the resulting HCSs. For instance, HCSs with uniform mesoporous shells have been synthesized by controlling the hydrolysis of tetraethyl orthosilicate and the polymerization of resorcinol and formaldehyde, followed by a pyrolysis-etching process.[66] The presence of mesopores within HCSs facilitates electromagnetic wave penetration and multiple reflections.[66] Moreover, multilayer HCSs can be synthesized by repeating sol–gel $SiO_2$ deposition and RF layer formation, as shown in the SEM and TEM images of double-layer HCSs in Fig. 2c–g.[65] A homogeneous porous carbon shell was successfully coated onto single-layer HCSs, and these multilayer structures exhibit increased void space, enlarged surface area, and higher density of active sites.

Despite the many advantages of HCSs, the energy density of hollow carbon-based electrochemical capacitors remains limited due to their reliance on electric double-layer capacitance. Introducing non-metal heteroatoms such as N, O, P, and B into carbon frameworks has proven to be an effective strategy to optimize the porous structure, increase the density of active sites, enlarge the surface area, and enhance the pseudocapacitive contribution.[67–69] Among these, N- and O-doped hollow carbon materials have been most extensively investigated, due to their facile preparation and ability to generate hierarchical porous structures.[16,28,37] As electrode materials, these materials often exhibit significantly improved capacitance. In general, N-doping can be achieved by incorporating N-rich precursors during the polymerization process, while O-doping can be introduced through chemical etching. In addition, B atoms can be incorporated into the porous carbon frameworks *via* high-temperature treatment, whereas P-doping is often accomplished through subsequent phosphating.[29] Collectively, these non-metal doped hollow carbon materials have been successfully developed and studied for diverse energy conversion applications.

The incorporation of heteroatoms into a carbon framework often significantly modifies the local electronic environment and disrupts the inherent electroneutrality of carbon materials. In the course of the oxygen reduction reaction, $sp^2$-hybridized carbon structures can generate $sp^3$-hybridized or defect sites, while simultaneously enhancing the effective participation of π electrons. These combined effects effectively boost the catalytic efficiency of the carbon-based electrocatalysts.[70] However, the phenomenon of "self-purification" often drives heteroatoms to redistribute across the material surface, leading to poor stoichiometric control of dopant concentration.[71] Instead of using conventional doping strategies (that includes sequential steps of pre-carbonization, activation, and heteroatom incorporation) which are inherently labour-intensive and time-consuming, it is recommended to utilize more straightforward facile synthetic approaches for producing the target sustainable and high-performance HCS electrocatalysts. For instance, Chen and colleagues developed a streamlined one-step strategy to synthesize HCSs through the pyrolysis of polypyrrole-coated polystyrene (PPy@PS) core–shell nanoparticles, followed by chemical activation of the HCSs utilizing KOH to yield an activated hollow carbon sphere (A-HCS) material which fits for electrode applications, delivering outstanding supercapacitor performance with a specific capacitance of 535 F $g^{-1}$ (Fig. 3).[38] According to Chen *et al.*, this A-HCS material having a high specific surface area coupled with hollow interiors exhibited well-defined porosity confined within an ultrathin curved carbon shell of less than 12 nm, as well as abundant N- and O-containing functional groups.[38] A comparative overview of the capacitance performance of some reported hollow carbon-based materials is shown in Table 1.

 

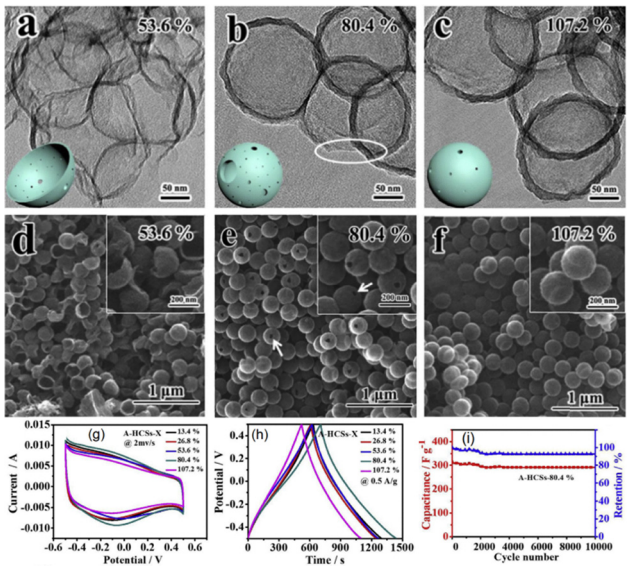


Fig. 3 TEM and SEM images of the reported (a) and (d) A-HCSs-53.6%; (b) and (e) A-HCSs-80.4%, and (c) and (f) A-HCSs-107.2%. The green-colored spherical insets in (a), (b), and (c) show the schematic illustration of HCSs. (g) CV curves of activated composites at 2 mV $s^{-1}$. (h) Galvanostatic charge–discharge curves obtained for activated composites in 6 M KOH electrolytes with a constant current density of 0.5 A $g^{-1}$. (i) Specific capacitance of A-HCSs-80.4% during charge–discharge cycles at current densities of 0.5 A $g^{-1}$ for the total of $10^4$ cycles. Reproduced from ref. 38 with permission. Copyright 2017 Elsevier.

Table 1 Specific capacitance comparison of reported HCS materials[38,72–78]

| Sample | Specific capacitance (F $g^{-1}$) | Ref. |
|---|---|---|
| Microporous HCSs | 240 (2 mV $s^{-1}$) | 72 |
| N and O doped HCSs | 210 (0.5 A $g^{-1}$) | 73 |
| N doped porous CSs | 388 (1 A $g^{-1}$) | 74 |
| Mesoporous HCSs | 253 (1 A $g^{-1}$) | 75 |
| Porous CSs | 260 (0.5 A $g^{-1}$) | 76 |
| Graphite HCSs | 273 (0.5 A $g^{-1}$) | 77 |
| Porous N-doped HCSs | 213 (0.5 A $g^{-1}$) | 78 |
| Hierarchical porous CSs | 401 (0.5 A $g^{-1}$) | 38 |

To further enhance device capacitance in the case of utilizing HCS materials in energy storage systems, the development of well-defined pore structures and the incorporation of heteroatoms into HCSs are often highly desirable. In this case, the relatively large specific surface area (of around 935 $m^2$ $g^{-1}$) and hierarchical porosity of the N- and O-doped HCSs fabricated by Chen *et al.* featuring macro-, micro-, and mesoporous structures collectively promoted the efficient ion and electron transport of the composite system.[38] Since the high heteroatom content contributes significant pseudocapacitance through redox faradaic reactions of the electrochemically active functional groups, the activated HCSs delivered excellent specific capacitance of 535 F $g^{-1}$ at a current density of 0.2 A $g^{-1}$, while still retaining 55% of their maximum capacitance at 10 A $g^{-1}$.[38] The activated heteroatom-doped HCSs combine high surface area, hierarchical porosity, and abundant functional groups to deliver excellent electrochemical performance.

## $MoS_2$ and HCS composite catalysts

$MoS_2$, a representative TMD, is often regarded as an inorganic analogue of graphene. The edge sites of $MoS_2$ (composed of exposed Mo and S atoms) often enable strong covalent bonding, whereas the interlayer S atoms are bound only *via* weak van der Waals interactions. Due to its stacking symmetry, $MoS_2$ can crystallize into three distinct polymorphs, tetragonal (1T-$MoS_2$), hexagonal (2H-$MoS_2$), and rhombohedral (3R-$MoS_2$).[64] In its monolayer form, $MoS_2$ often consists of a molybdenum layer sandwiched between two S layers, with each Mo atom coordinated to six S atoms in a trigonal prismatic geometry.[79] In general, the electronic structure and catalytic behaviour of $MoS_2$ are highly dependent on its phase composition, with the 2H phase exhibiting semiconducting properties, while the 1T phase is considered to be metallic.[80] The electrochemical activity is likewise phase sensitive.[14] Specifically, 1T-$MoS_2$ adopts an octahedral coordination derived from a trigonal prism rotated by 60° around the *c*-axis.[81] The partially occupied Mo 4d and S 3p orbitals near the Fermi level activate the basal planes of 1T-$MoS_2$, generating abundant catalytic sites for hydrogen generation. As a result, 1T-$MoS_2$ often demonstrates superior catalytic performance compared to 2H-$MoS_2$ and is widely considered a promising bifunctional electrocatalyst. Notably, prior studies have shown that the basal-plane activity of 1T-$MoS_2$ yields a conductivity approximately 107 times higher than its 2H counterpart.[82,83]

$MoS_2$ nanosheets have emerged as promising alternatives to platinum for HER application. Numerous strategies have been investigated to further enhance the catalytic efficiency of $MoS_2$ nanosheets, aiming to increase the density of their active sites, improve structural stability, and optimize hydrogen adsorption. Nevertheless, the OER activity of 1T-$MoS_2$ nanosheets remains relatively weak.[16,27] Considerable efforts have therefore been devoted to boosting their overall electrochemical performance.[50] For instance, interface engineering and the incorporation of metal atoms into otherwise inert planes have been explored as effective approaches for $MoS_2$-based catalysts.[64,65] Hybrid composites of $MoS_2$ with conductive metals or alloys have also been shown to accelerate charge transport, generate supplementary active sites, and enhance durability. Carbonaceous materials can also serve as excellent support for the $MoS_2$ nanosheet components, enabling synergistic improvements in both HER and OER activity. Key design principles have thus centered on maximizing active site exposure, facilitating electron transport, and inducing favorable phase transitions in $MoS_2$.

To overcome these above-mentioned issues, $MoS_2$ nanosheets have been integrated with conductive substrates to form diverse heterostructures aimed at boosting their electrochemical performance. Carbon-based materials including graphene, reduced graphene oxide, carbon nanotubes, and HCSs have been extensively investigated in this context.[16,35] Among these options, HCSs have attracted particular interest due to their high porosity, well-defined internal cavities, excellent thermal stability, and superior electrical conductivity.[64] In comparison with carbon nanotubes, HCSs exhibit a distinctive pore structure

that could provide abundant anchoring sites for $MoS_2$ nanosheets while accommodating the volume fluctuations during prolonged cycling processes. Consequently, the combination of $MoS_2$ nanosheets with the high surface area and low density of HCSs enhances the ion/electron transport, energy storage capability, and catalytic activity of the material, making them highly promising for advanced electrochemical applications.

Considering the phase structure of $MoS_2$, the hydrothermal synthesis route offers distinct advantages, including high crystallinity and uniform particle size distribution, due to its mild operating conditions compared to chemical vapor deposition, electrochemical, or other chemical methods.[84,85] Preparation parameters *e.g.*, reaction time, solvent choice, and the incorporation of ionic liquids strongly influence the morphology and phase purity of $MoS_2$.[64] For instance, Tian and co-workers demonstrated phase purity control within a pH range of 5–8; Lee *et al.* synthesized composite catalysts across a broad pH spectrum for property comparison; and Li's group systematically investigated the combined effects of pH and solvent environment.[86–88] Recently, Liu and co-workers synthesized a composite material having enhanced HER and supercapacitor performance with homogeneous growth of $MoS_2$ nanosheets on HCSs.[64] In this approach, hybrid $MoS_2$/HCSs composites (CMS-*x*-*y* in Fig. 4, where *x* represents the weight ratio of $Na_2MoO_4 \cdot 2H_2O$ and *y* corresponds to the pH value) were synthesized *via* a solvothermal route to uniformly anchor $MoS_2$ nanosheets onto HCSs.[64] Notably, the CMS-20-3.5 composites exhibited a mixed 1T/2H phase structure, delivering high energy density when assembled with activated carbon into an asymmetric supercapacitor device.

Based on the TEM images (at varying magnifications) of the CMS-20-3.5 composite catalyst presented in Fig. 4a–c, the thin $MoS_2$ nanosheets were vertically and uniformly grown on HCS substrate without noticeable aggregation.[64] This homogeneous distribution was attributed to the co-presence of ethanol and water within a pH range of 3–4, where the increased concentration of $H^+$ ions promoted hydrolysis of the S precursor and enhanced solvent acidity.[64] Such uniform growth maximized the utilization of $MoS_2$ active sites, while the thin carbon layer of HCSs facilitated charge transport within the composite system, thereby improving catalytic performance. The LSV curves in Fig. 4d demonstrated that the CMS-20-3.5 composite exhibited the highest HER activity using optimized parameters, and the fact that the electrode prepared from CMS-20-3.5 showed the lowest Tafel slope (of 51.0 mV $dec^{-1}$) indicated the superior reaction kinetics of the material.[64] In addition, the $C_{dl}$ value derived from CV measurements at different sweep rates (Fig. 4c) confirmed that CMS-20-3.5 also exhibited the largest capacitance of 27.30 mF $cm^{-2}$ in this case.[64]

The Tafel slopes of the HCSs@$MoS_2$ composite catalysts showed a clear correlation with the LSV curves, with values around 62 mV $dec^{-1}$, indicating that all the corresponding composites followed a similar reaction pathway.[64] This HCS composite fabricated by Liu *et al.* demonstrated much higher HER activity and a lower Tafel slope compared to its pure $MoS_2$ nanosheets counterpart, because of the improved conductivity

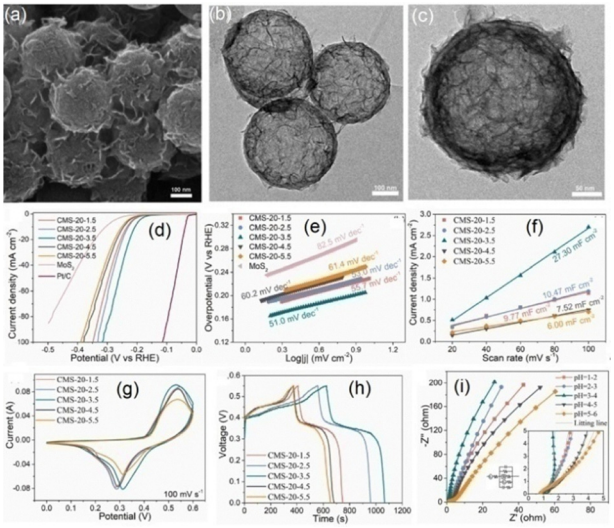


Fig. 4 (a)–(c) TEM images of $MOS_2$ modified HCSs (denoted as CMS-20-3.5). (d)–(i) Electrochemical performance of CMS-*x*-*y* composites in 0.5 M $H_2SO_4$ media: (d) LSV curves, (e) Tafel plots, (f) $C_{dl}$ values, (g) CV curves of the composite catalysts at a scan rate of 100 mV $s^{-1}$, (h) GCD curves of the composites at a current density of 1 A $g^{-1}$, and (i) Nyquist plots of the composites with the inset demonstrating the corresponding equivalent circuit diagram. Reproduced from ref. 64 with permission. Copyright 2025 Elsevier.

that was due to the presence of HCSs and the prevention of $MoS_2$ stacking, which exposed a greater number of active sites. During $H_2$ generation in acidic media, the Volmer step (eqn (1)) involving proton adsorption on the $MoS_2$ surface occurred first, followed by the rate-determining Heyrovsky step (eqn (2)) for $H_2$ desorption.[64] The hollow carbon shells were able to increase the number of accessible active sites while promoting efficient electron transport from the carbon framework to $MoS_2$ through strong coupling interactions, thereby facilitating the overall $H_2$ evolution process.

$$H_3O^+ + e^- \rightarrow H_{ads} + H_2O \quad (1)$$

$$H_{ads} + H_3O^+ + e^- \rightarrow H_2 + H_2O \quad (2)$$

The electrochemical energy storage behaviour of this HCSs@$MoS_2$ composite material was further examined by Liu *et al.* through CV, GCD, and EIS analyses.[64] As shown in Fig. 4d and g, the CV and GCD profiles of the electrodes at varying scan rates demonstrated that increasing the scan rate led to a progressive rise in peak current, indicative of excellent kinetic reversibility and robust rate capability. The observed broadening of the oxidation peak toward higher potentials and the shift of the reduction peak toward lower potentials were because of the electrode polarization effects.[64,89,90] In this case, the CMS-20-3.5 composites also exhibited the largest current response and the most pronounced CV enclosed area, underscoring its superior specific capacitance. Complementary EIS measurements (Fig. 4f) further corroborated these findings. All composites fabricated displayed characteristic pseudosemicircles in the high-frequency region and distinct slopes in the low-frequency domain, in which CMS-20-3.5 showed the

 

smallest semicircle diameter and steepest slope, signifying reduced charge transfer resistance, enhanced ion diffusion, and accelerated transport kinetics.[64] Collectively, these features highlighted the pivotal role of hollow carbon shells in optimizing the capacitive performance of $MoS_2$ modified composites. In addition, an asymmetric supercapacitor was assembled by Liu and co-workers using CMS-20-3.5 and active carbon (AC) in 3 M KOH electrolyte.[64] The estimated $C_{dl}$ value of CMS-20-3.5||AC was 102.5 F $g^{-1}$ at 1 A $g^{-1}$ with reasonably high stability maintained even after 5000 cycles. This device also achieved an excellent maximum energy density of 36.4 Wh $kg^{-1}$ at a corresponding power density of 800 W $kg^{-1}$, attributed to the intrinsic high stability of the HCSs@$MoS_2$ composites.[64] The hollow carbon shells provided mechanical resilience against deformation arising from repeated expansion and contraction during long-term charge–discharge cycling. Moreover, serving as a robust substrate, the HCSs were able to effectively mitigate the aggregation of $MoS_2$ with its lamellar structure, preserving accessible active sites and enhancing the electrochemical efficiency of the composite material.[64]

Precise control over synthesis has been critical in the case of HCS-based $MoS_2$ modified composite catalysts to achieving satisfied performance. The porous structure of HCSs provides abundant nucleation sites for $MoS_2$ deposition while the incorporation of non-metal dopants into the carbon framework further introduces active centres for $MoS_2$ growth.[91–94] Wei and co-workers demonstrated a controllable strategy for constructing P-doped $MoS_2$ nanopetals on N-doped HCSs (as shown in the TEM images in Fig. 5a–i), yielding enhanced $H_2$ generation efficiency.[37] By tuning relevant synthetic parameters, layered $MoS_2$ nanopetals were able to be directed to grow either on the exterior or within the hollow carbon shells.[37] The hierarchical N-C@P-$MoS_2$ core–shell structures (fabricated by Wei *et al. via* calcination and hydrothermal treatment) exhibited superior conductivity and much higher density of active sites.[37] These composites delivered outstanding HER performance, characterized by a low onset overpotential (117 mV), a small Tafel slope (68 mV $dec^{-1}$), and excellent stability, because of the synergistic effects of the $MoS_2$ and HCS components in a rationally engineered hierarchical structure.

The porous structure and thin carbon shells of HCSs again were advantageous for enhancing the conductivity of the composites and facilitating free diffusion of reactants during electrochemical processes. The TEM analysis in Fig. 5f revealed that the P-$MoS_2$ nanosheets exhibited fewer layers with increased interplanar spacing (0.67–0.72 nm, Fig. 5g). This enlargement of the (002) plane in 2H-$MoS_2$ offered additional active sites for $H_2$ adsorption and desorption.[7,37,94,95] In addition, Wei *et al.* also successfully encapsulated P-doped $MoS_2$ nanosheets inside the N-doped HCSs (N-C/P-$MoS_2$) by adjusting precursor loading (Fig. 5h–i). However, in this case, the confinement of the active sites within the carbon shells hindered accessibility, resulting in diminished HER activity of the composites.[37] These further confirmed the high dependency of electrocatalytic activity of $MoS_2$ modified HCS composites on structural configuration, particularly the exposure of active sites and overall conductivity, with non-metal doping emerging as a powerful strategy to optimize the electrochemical performance of this hybrid system.

Detailed HER and relevant data provided by Wei and co-workers are presented in Fig. 6, with the HER polarization curves of C@$MoS_2$, N-C@$MoS_2$, and N-C@P-$MoS_2$ (Fig. 6a) highlighting the pronounced influence of heteroatom doping.[37] Compared to the undoped system (C@$MoS_2$), N-C@$MoS_2$ exhibited significantly enhanced activity. This was because the introduction of N heteroatoms modified the electronic configuration by inducing irregular charge distribution around adjacent carbon atoms, improving the intrinsic conductivity of the material. Moreover, substitution of P atoms for S atoms in the basal plane altered the electronic environment of the neighbouring S atoms, effectively tuning the conductivity of the material. In this case, the P atoms acted as the new catalytic centres, expanding the interlayer spacing and increasing the density of accessible active sites.[37] The synergistic contribution of N and P dopants in facilitating $H_2$ production is illustrated in the proposed reaction pathways for N-C@P-$MoS_2$ composites in Fig. 6e. Since the P-doped $MoS_2$ nanosheet modified N-doped HCSs (N-C@P-$MoS_2$-2) delivered the most outstanding performance (with a low onset overpotential of 117 mV, an overpotential of 188 mV at 10 mA $cm^{-2}$ and higher current densities under identical potentials), it was clear that dual N and P doping played a pivotal role in optimizing the conductivity and increasing the active site density of the $MoS_2$ modified HCS system.[37]

Among the various HCSs, double-layer HCSs (DLHCs) can be fabricated *via* a $SiO_2$-templated approach by tuning the deposition and polymerization steps. Compared with single-layer DCSs, DLHCs often exhibit a more uniform morphology, and

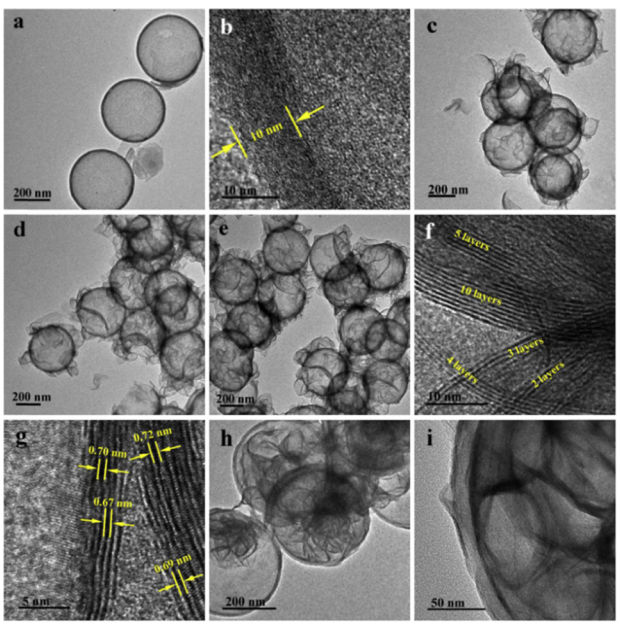


Fig. 5 TEM images collected for (a) N-doped HCSs, (c) C@$MoS_2$-2, (d) N-C@$MoS_2$-2, (e) N-C@P-$MoS_2$-2, and (h) and (i) N-C/P-$MoS_2$-2 (inside decoration) composite systems. High-resolution TEM images of (b) N-doped HCSs, and (f) and (g) N-C@P-$MoS_2$-2 composites. Reproduced from ref. 37 with permission. Copyright 2019 Elsevier.

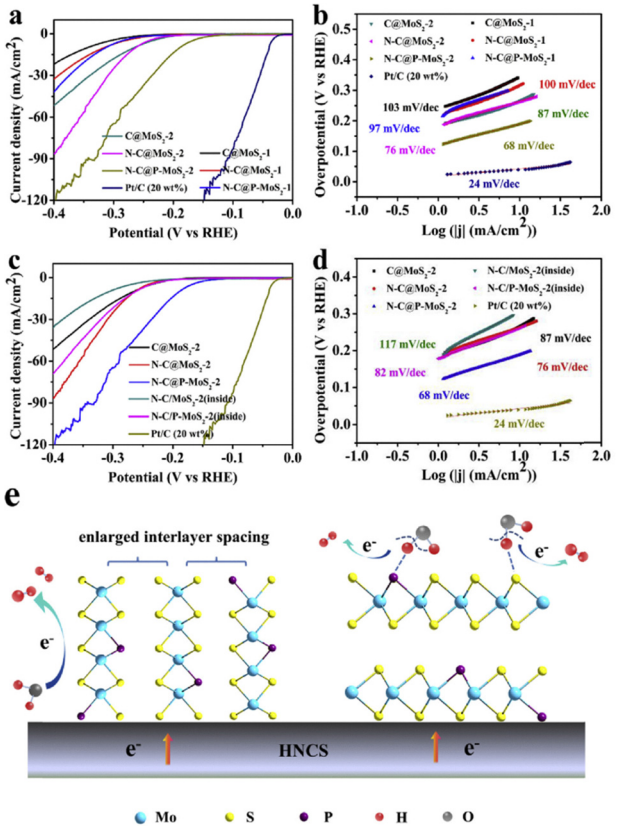


Fig. 6 (a) Detailed HER polarization curves of the composite catalysts at a scan rate of 5 mV $s^{-1}$. (b) Corresponding Tafel plots derived from the HER polarization curves. (c) HER polarization curves of the composite systems, and (d) corresponding Tafel plots. (e) Proposed reaction mechanism for $H_2$ generation using the N-C@P-$MoS_2$ system. Reproduced from ref. 37 with permission. Copyright 2019 Elsevier.

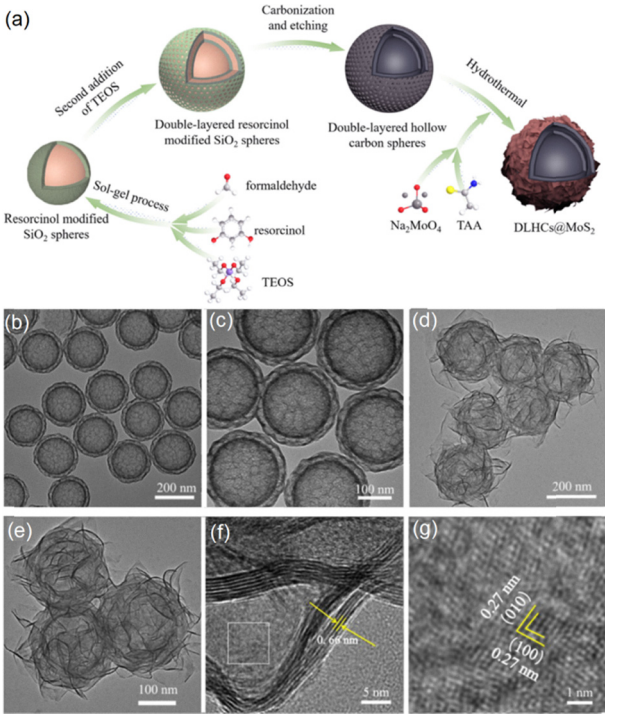


Fig. 7 (a) Detailed synthetic processes for $MoS_2$ nanosheet modified DLHCs. (b) and (c) TEM images of the DLHCs substrate. (d)–(g) TEM images of the DLHCs@$MoS_2$-1 composites at different magnifications, with (g) showing the region highlighted by the white box in (f). Reproduced with permission from ref. 35. Copyright 2022 Elsevier.

both their inner and outer carbon shells exhibit rough and porous surfaces that offer abundant nucleation sites for loading TMDs.[96] DLHCs thus are considered promising hosts for growing TMDs to enhance energy storage performance and rate capability. Luan *et al.* developed a core–shell $MoS_2$ decorated DLHC composite material (DLHCs@$MoS_2$ in Fig. 7) having synergistic enhancement in electrochemical activity; exhibiting low Tafel slope, small onset potential, and outstanding supercapacitor performance (delivering a high specific capacitance of 399.4 F $g^{-1}$ at a current density of 0.5 A $g^{-1}$).[35] In this case, the DLHC framework provided excellent structural stability, inhibited the aggregation of $MoS_2$ nanosheets, increased the exposure of active sites, and enhanced the electrical conductivity of the composite system.[35] As illustrated in Fig. 7a, a RF polymer layer was sequentially deposited twice onto sol–gel-derived $SiO_2$ spheres, followed by subsequent removal of the silica template using NaOH to yield a well-defined highly porous DLHC substrate (Fig. 7b and c, with an interlayer spacing of approximately 18 nm between the two carbon shells).[35] The $MoS_2$ nanosheet components were then uniformly coated onto the DLHC surfaces *via* hydrothermal treatment, producing a distinct core–shell structure (Fig. 7d and e), with $MoS_2$ nanosheets adhered tightly to the DLHCs surface, forming a robust and continuous shell.[35]

According to Luan *et al.*, the $MoS_2$ nanosheets were determined to consist of 8–12 layers, and the measured interlayer distance of 0.66 nm for the (002) planes confirmed the formation of the 2H-phase $MoS_2$.[35,47,97,98] The magnified region highlighted in Fig. 7f and shown in Fig. 7g displays the characteristic honeycomb lattice corresponding to the (010) and (100) planes, further verifying the crystalline structure.

The analysis of the X-ray absorption near-edge structure (XANES) and X-ray absorption fine structure (XAFS) spectra (Fig. 8a and b) shows that the Mo K-edge of the DLHCs@$MoS_2$-1 composites shifts to higher energy relative to pristine $MoS_2$, demonstrating the stronger electronic interaction between $MoS_2$ and the DLHC base, arising from the electron transport at the interfaces.[13,35,99] In addition, differences between the spectra of DLHCs@$MoS_2$-1 and metallic Mo confirmed the presence of a Mo–O–C heterointerface which originated from carbonyl groups formed during NaOH etching. The HER data of the DLHCs@$MoS_2$ composites with varying $MoS_2$ loading presented in Fig. 8c and d demonstrated that as the amount of assembled $MoS_2$ nanosheets increased, the onset potential became progressively more negative, indicating a decline in catalytic activity. This trend was particularly evident for the DLHCs@$MoS_2$-1.5 and DLHCs@$MoS_2$-2 composites, both of which exhibited larger onset potentials, reflecting reduced HER performance.

According to Luan *et al.*, the behaviour described above was due to the intrinsic characteristics of $MoS_2$. Since $MoS_2$ exposes

 

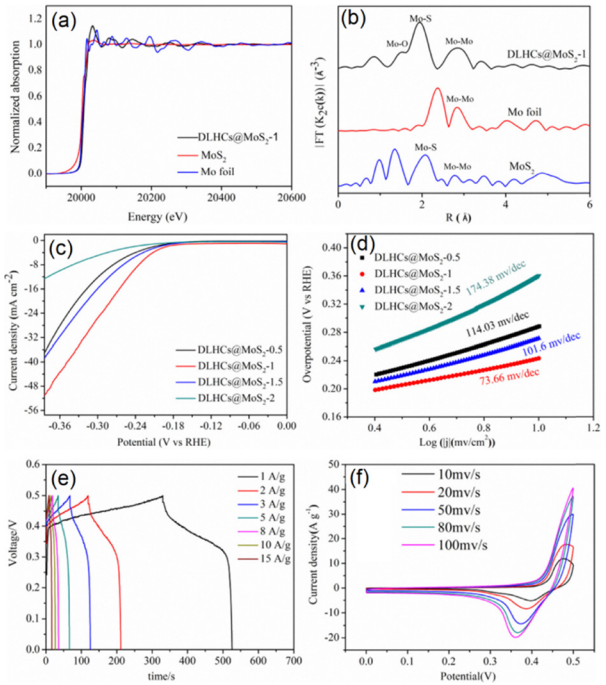


Fig. 8 Data on the chemical environment of the DLHCs@$MoS_2$-1 composites as probed *via* X-ray absorption spectroscopy: (a) Mo K-edge spectra of the EXAFS spectra; (b) Fourier transform of EXAFS spectra. (c) LSV curves and (d) Tafel slopes of the DLHCs@$MoS_2$ composite systems. (e) and (f) Data collected using the DLHCs@$MoS_2$-1 electrode: (e) GCD curves collected at different current densities and (f) CV curves at varying scan rates. Reproduced with permission from ref. 35. Copyright 2022 Elsevier.

active sites primarily along its S edges, its ultrathin nanosheet structure tends to agglomerate easily and suffers from limited stability.[27] When $MoS_2$ is integrated with DLHCs, however, a greater number of S edge sites become accessible.[37] Both insufficient and excessive loading of $MoS_2$ nanosheets reduced the number of effectively exposed active sites, diminishing the overall catalytic performance.[100] Moreover, the Tafel relationship describing the correlation between $H_2$ generation overpotential and current density can be expressed as shown in eqn (3).

$$\eta = b\log j + a \quad (3)$$

where $b$ corresponds to the Tafel slope which reflects the intrinsic kinetics of the HER process. The commonly accepted HER pathways include the Volmer–Heyrovsky and Volmer–Tafel mechanisms. The decrease in Tafel slope (from 174.4 to 74.7 mV $dec^{-1}$) in Fig. 8d indicates that the rate-determining step of the HER follows the Heyrovsky (electrochemical desorption) reaction.[35,37]

The GCD and CV curves in Fig. 8e and f show an increased current density and extended charge–discharge times of the composite system.[35] In this case, the CV profiles exhibit distinct redox peaks corresponding to the reversible changes in the valence state of Mo (Mo(IV) ⇔ Mo(V) ⇔ Mo(VI)), which significantly enhances the capacitance performance of the composites. The presence of DLHC components facilitates charge transport to the active sites on the $MoS_2$ components with promoted electrochemical reactions, and the hierarchical core–shell structure enhances the structural stability of the material. When utilized as supercapacitor electrodes, $MoS_2$ nanosheets anchored on DLHCs expand the electrolyte–electrode interfaces, expose a higher density of electrochemically active sites, and consequently enhance the energy storage capacity of the material.

## MoSSe components on HCSs as catalysts

To substantially enhance the performance of $MoS_2$/HCS composites, researchers often employ $MoS_2$-based alloys and heterostructure construction methodologies, which can increase the density of active sites through interface engineering.[49] Due to the structural similarity to $MoS_2$, $MoSe_2$ has been another popular option for electrocatalyst fabrication, featuring a low Gibbs free energy for hydrogen adsorption. Its graphite-like layered structure, characterized by relatively wide interlayer spacing, is believed to facilitate charge transport through enhanced interlayer reflection and scattering. Nevertheless, the intrinsically low conductivity of $MoSe_2$, along with its tendency to aggregate, often diminishes its catalytic efficiency, while its substantial volume expansion often further impedes mass transfer.[101] Integrating layered $MoSe_2$ with $MoS_2$ to form heterostructures or alloyed structures is therefore a promising strategy. In this case, the incorporation of Se can enrich active sites and improve overall water splitting performance.[102] When $MoSe_2$ is anchored onto HCSs, its volume expansion can be effectively constrained, boosting the pseudocapacitive behaviour of the HCSs.[103] Recent research has increasingly focused on constructing Se-doped $MoS_2$ (MoSSe) composites on HCSs, where compositional tuning of MoSSe provides a versatile platform for developing high-performance catalysts.

In general, $MoSe_2$ features a graphite-like layered structure with relatively large interlayer spacing, where each Mo atomic layer sandwiched between two Se layers through strong intralayer covalent bonding and weak interlayer van der Waals interactions. This structural arrangement governs its intrinsic electronic properties, and its electrocatalytic activity is primarily associated with exposed Mo centres and Se-terminated edge sites.[49] A range of reported $MoSe_2$-based composites have demonstrated promising functional performance, for example, $MoSe_2$/N-doped carbon anodes showed stable and efficient behaviour in sodium-ion batteries, while 2H/1T-$MoSe_2$@graphene hybrids exhibited enhanced microwave absorption capabilities.[101,103,104] However, both $MoS_2$ and $MoSe_2$ often exhibit rapid growth tendencies during synthetic processes, making it difficult to achieve homogeneous dispersion while avoiding aggregation. In such cases, employing HCSs as the base forming composite materials can be considered a practical solution. The tunable composition and surface chemistry of HCSs can regulate the nucleation and growth kinetics of $MoS_2$

and $MoSe_2$, while simultaneously offering efficient pathways for charge transport and mass diffusion. As a result, the incorporation of $MoS_2$/$MoSe_2$ composite nanocomponents onto the HCS framework leads to more exposed active sites and significantly enhanced energy storage performance.

The controlled growth of $MoS_2$/$MoSe_2$ composite nanosheets on HCSs has been widely explored as an effective strategy to enhance structural uniformity and catalytic performance. Yang and co-workers, for instance, employed $SiO_2$ templates to fabricate HCSs and deposited $MoS_{2-2x}Se_{2x}$ nanosheets with uniform spatial distribution onto this HCS base *via* a hydrothermal process.[50] In this system, both the precursor concentration and the Se/S precursor ratio were found to be critical parameters governing the nucleation, deposition behaviour, and overall growth kinetics of $MoS_2$ and $MoSe_2$ on the carbon-based framework. Representative TEM images of the constructed $MoS_{2-2x}Se_{2x}$/HCSs composites (denoted C@$MoS_{1.8}Se_{0.2}$) are shown in Fig. 9a–d, confirming that the HCSs exhibit a consistent and well-defined size distribution conducive to homogeneous nanosheets assembly.

The C@$MoS_{1.8}Se_{0.2}$ composites in Fig. 9 exhibit an average particle diameter of approximately 250 nm. As shown in the HRTEM image in Fig. 9, the $MoS_{2-2x}Se_{2x}$ nanosheets are uniformly distributed and conformally anchored onto the surfaces of the HCSs.[50] In contrast to the $MoS_2$ modified HCSs presented in Fig. 5 and 7, the $MoS_{2-2x}Se_{2x}$ nanosheet composites displayed much improved interfacial contact with the HCS substrates, which was attributed to the distinct growth behaviour induced by the incorporation of Se components. The presence of Se increased the density of nucleation sites, facilitating more effective deposition and co-growth of $MoS_2$ and $MoSe_2$ monomeric species.

The composite nanosheets grow both vertically and horizontally on the HCS surfaces, forming a well-integrated heterostructure, with the Se-doped $MoS_2$ layers exhibiting an expanded interlayer spacing of 0.71 nm (Fig. 9c). Fig. 9d further presents a TEM image showing nanosheets lying horizontally on the HCS surface, where the characteristic honeycomb lattice of $MoS_2$ is clearly resolved, with lattice spacings corresponding to the (100) and (010) planes. Notably, the interlayer spacing of the Se-doped structure was significantly larger than that of pristine 2H-$MoS_2$.[49,50] This expansion increased the exposure of catalytically active sites and was advantageous for promoting hydrogen adsorption and desorption during the hydrogen generation reactions. In this case, the enlarged interlayer spacing generated by Se incorporation increased the number of accessible catalytic sites and facilitated charge transport, thus enhanced the electrocatalytic activity of the $MoS_{2-2x}Se_{2x}$ modified HCS system. The composition of the $MoS_{2-2x}Se_{2x}$ nanosheet components could be precisely tuned by adjusting the relative amounts of S and Se precursors.[50] According to Yang *et al.*, when the Se/S molar ratio was set to 0.1, the resulting C@$MoS_{2-2x}Se_{2x}$ composite system exhibited the lowest overpotential and the smallest Tafel slope among the tested samples.[50] As shown in the durability and operational stability related HER data in Fig. 9e, the polarization curve of the composites after 1500 cycles showed only a slight increase in onset overpotential, indicating that the rate of $H_2$ production remains essentially unchanged with the catalytic behaviour of the material largely preserved.[50] The time-dependent current density profile over 20 h (Fig. 9f) with only minimal decay demonstrated that the composite catalyst maintained stable activity in acidic media and remained robust at a constant applied potential.[50]

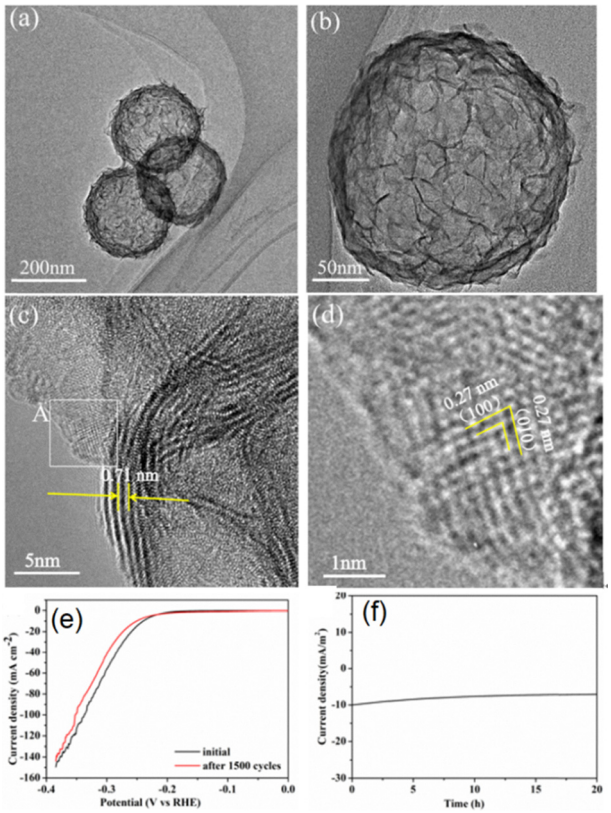


Fig. 9 (a)–(c) TEM images of the reported C@$MoS_{1.8}Se_{0.2}$ composites; (d) corresponding enlarged white square area in (c); (e) HER polarization data for C@$MoS_{1.8}Se_{0.2}$ composites before/after 1500 cycles; (f) time-dependent current density curve for the C@$MoS_{1.8}Se_{0.2}$ composites at a static overpotential of 190 mV *vs.* reversible hydrogen electrode for 20 h. Reproduced with permission from ref. 50. Copyright 2021 American Chemical Society.

MoSSe modified HCS systems are also popular choices for lithium–sulfur battery applications. Graphitic carbon materials with hollow structures offer several advantages for lithium–sulfur batteries, including the ability to accommodate high sulfur loadings, buffer the substantial volume expansion of sulfur during cycling, and suppress the shuttling of lithium polysulfides (LiPSs).[105,106] Elemental doping in this case can further enhance the performance of these carbon hosts by modulating their electronic band structures and density of states, improving the catalytic activity of the composites towards LiPSs conversion.[51] Such doping also promotes the formation of the conductive 1T-$MoS_2$ phase and introduces S vacancies, collectively enhancing charge transport and overall conversion kinetics. Zhang *et al.* demonstrated these principles by growing MoSSe nanosheets on N-doped HCSs (MoSSe/NC in

 

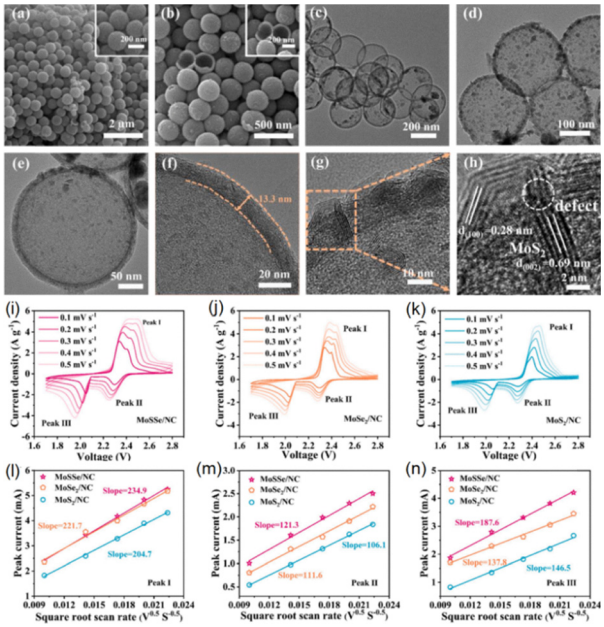


Fig. 10 (a) and (b) SEM images of the MoSSe/NC system. (c)–(h) TEM images of MoSSe/NC collected at different magnifications. (i)–(k) CV curves of the MoSSe/NC, $MoSe_2$/NC, and $MoS_2$/NC composite systems at varying scan rates ranging from 0.1–0.5 mV $s^{-1}$. (l)–(n) Logarithmic peak current *versus* logarithmic scan rate of the corresponding peaks. Reproduced with permission from ref. 51. Copyright 2023 Elsevier.

Fig. 10) for use as both the S host and separator modification, enabling efficient catalytic adsorption and conversion of LiPSs.[51] When employed as an S host, the MoSSe/NC composite system significantly improved electron and ion transport while mitigating S volume expansion, leading to accelerated redox kinetics. Based on the SEM (Fig. 10a and b) and TEM (Fig. 10c–e) observation, it was confirmed that the MoSSe/NC composites maintained a uniform, monodisperse hollow morphology, with MoSSe nanosheets (having a moderate loading amount to avoid excessive aggregation) evenly distributed across the HCS surfaces. The HRTEM analysis in Fig. 10f–h reveals a carbon shell of approximately 13.3 nm thick, which functions as both a mechanical buffer and a conductive framework to facilitate reaction kinetics and accommodate volume changes.[51] The few layered MoSSe/NC composites having an interlayer spacing of 0.69 nm along the (002) plane (which was larger than that of pristine $MoS_2$) showed expanded spacing that was beneficial for alleviating structural strain associated with $Li^+$ insertion and contributed to the improved electrochemical stability of the composite system.[51]

The diffusion behaviour and oxidation kinetics of $Li^+$ ions in the MoSSe/NC composite were also evaluated by Zhang and co-workers (Fig. 10i–k). The oxidation and reduction peak currents exhibited a linear dependence on the square root of the scan rate (Fig. 10l–n), demonstrating a diffusion-controlled electrochemical process. In this case, the $Li^+$ diffusion rate was affected by variations in electrolyte viscosity arising from the dissolution of LiPSs and the subsequent deposition of $Li_2S_2$/$Li_2S$ on electrode surfaces.[51] Due to the introduction of Se (together with expanded interlayer spacing and generated structural defects), the constructed MoSSe/NC system showed quite high $Li^+$ diffusion rates across multiple reaction pathways. According to Zhang *et al.*, the MoSSe/NC modified separator contributed to interfacial charge modulation and increased the number of exposed active sites, resulting in facilitated rapid anchoring and catalytic conversion of LiPSs with much improved uniform $Li_2S$ deposition.[51]

## Co and Ni sulfide modified $MoS_2$ composites on HCS as catalysts

Transition metal sulfides such as Co and Ni sulfides, along with their complexes, have attracted considerable interest as electrode materials for supercapacitors due to their high electrical conductivity and pronounced electrochemical activity. Because the crystal structures of $MoS_2$ differ substantially from those of Ni- and Co-based sulfides, incorporating Ni or Co sulfides into $MoS_2$ frameworks requires careful control to achieve a homogeneous distribution. Consequently, developing reliable synthetic strategies for Ni and Co sulfides involved systems remains a significant challenge. When combined with $MoS_2$, the formation of heterostructures becomes essential due to the structural differences between the two components. Co- and Ni-based sulfides integrated with $MoS_2$ have been widely investigated for their robust redox behaviour and enhanced electroactivity.[107] For instance, among the various Co sulfides, $Co_9S_8$ has received particular attention because of its exceptionally high theoretical capacitance (5449 F $g^{-1}$).[108] $Co_9S_8$–$MoS_2$ heterostructures, which leverage synergistic interactions between the two phases, have been reported to deliver promising performance in supercapacitor applications.[109]

Liu *et al.* synthesized yolk–shell structured $Co_9S_8$–$MoS_2$ nanosheet alloy modified HCSs composites (using $SiO_2$ templates, $Co_9S_8$–$MoS_2$ NSA@HCS, as shown in Fig. 11) with superior capacitive behaviour and cyclic stability in hybrid supercapacitors.[7] The $Co_9S_8$–$MoS_2$ precursor nanosheets were uniformly distributed across the HCS surface, exhibiting an average diameter of approximately 600 nm. According to Liu *et al.*, the resulting $Co_9S_8$–$MoS_2$ NSA@HCSs after sulfurization developed a nanoflower-like morphology, with nanosheets noticeably thinner than those of the original cobalt–molybdate silicate precursor.[7] This $Co_9S_8$–$MoS_2$ nanosheet array deposited HCS material with a constructed yolk–shell structure showed much enhanced electrical conductivity, cyclic durability and capacitive performance.[7]

Some of the detailed electrochemical evaluation data collected by Liu *et al.* on the $Co_9S_8$–$MoS_2$ NSA@HCSs electrode is presented in Fig. 11. As shown in Fig. 11a, the $Co_9S_8$–$MoS_2$@HCSs composite exhibited two pairs of redox peaks at 0.37/0.29 V and 0.40/0.29 V, which were shifted to lower potentials compared to that of $Co_9S_8$–$MoS_2$.[7] This decrease in redox peak potentials was associated with the incorporation of the highly conductive HCSs substrate, which significantly facilitated charge transport of the composite system.[7] The redox features arising from

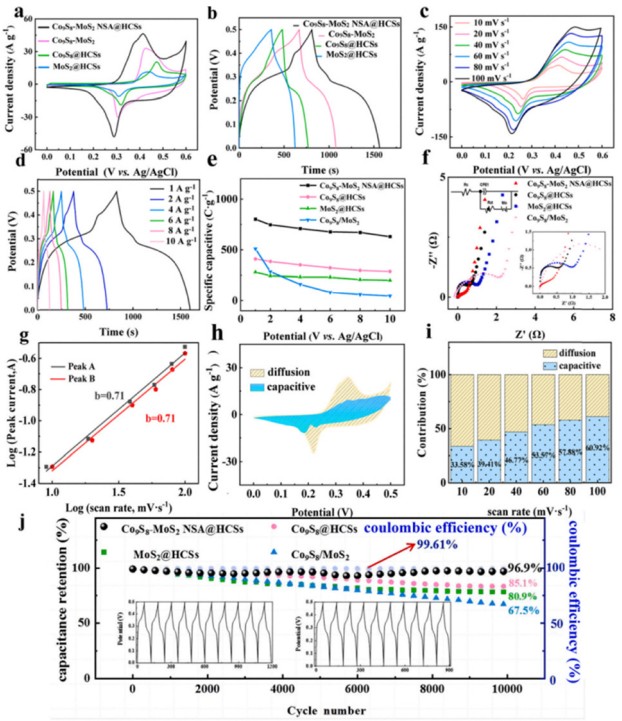


Fig. 11 (a) CV curves of $Co_9S_8$ and $MoS_2$ incorporated composite systems at 10 mV $s^{-1}$; (b) GCD curves of $Co_9S_8$ and $MoS_2$ incorporated composite systems at 1 A $g^{-1}$; (c) CV curves at 10–100 mV $s^{-1}$; (d) GCD curves at 1–10 A $g^{-1}$; (e) capacity values obtained using GCD curves at different current densities. Data on (f) EIS curves and electrode equivalent circuits of the composite systems, (g) *b*-values, and (h) capacitive and diffusion-controlled contribution curves (at 10 mV $s^{-1}$), and (i) relative contributions of capacitive and diffusion-controlled processes at various scan rates. (j) Comparison of cyclic stability and the corresponding coulombic efficiency at a current density of 10 A $g^{-1}$. Reproduced with permission from ref. 7. Copyright 2024 Elsevier.

the reversible oxidation and reduction of $Co^{2+}/Co^{3+}$ and $Mo^{3+}/Mo^{4+}$ in the presence of $OH^-$ can be described by eqn (4)–(7) below.[7]

$$MoS_2 + OH^- \leftrightarrow MoS_2OH + e^- \quad (4)$$

$$MoS_2OH + OH^- \leftrightarrow MoS_2O + H_2O + e^- \quad (5)$$

$$Co_9S_8 + OH^- \leftrightarrow Co_9S_8OH + e^- \quad (6)$$

$$Co_9S_8OH + OH^- \leftrightarrow Co_9S_8O + H_2O + e^- \quad (7)$$

In this case, the composite electrode showed the largest CV curve area, indicating its highest specific capacity and superior energy storage capability among all relevant composite samples.[7] Consistently, the GCD profiles in Fig. 11b show that the $Co_9S_8$–$MoS_2$NSA@HCS electrode delivered the longest discharge time, confirming its maximum specific capacity. The enhanced electrochemical activity of the composite system was further supported by the data presented in Fig. 11c–i, with the Nyquist plots (Fig. 11f) having the charge transport resistance ($R_{ct}$) corresponding to the semicircle radius in the high-frequency region and the intercept at the *x*-axis representing the solution resistance ($R_s$) between the electrolyte and electrode.[7] Based on the cyclic stability of the material evaluated at the current density of 10 A $g^{-1}$ (Fig. 11j), the $Co_9S_8$–$MoS_2$ NSA@HCSs electrode retained 96.9% of its initial capacity after 10 000 charge–discharge cycles with negligible distortion in curve shape.[7] It was clear that integrating $Co_9S_8$ and $MoS_2$ onto HCSs could significantly enhance the electrochemical activity of the composite system for energy conversion/storage applications.

Among the variety of transition metal candidates, Ni incorporated materials are often considered hot choices for electrocatalyst fabrication due to their reliable catalytic properties. Layered $NiS_2$, in particular, shares structural similarities with $MoS_2$ and has therefore been frequently investigated for constructing $NiS_2/MoS_2$ hybrid systems for use in energy storage/conversion and related fields. Luan *et al.* reported the fabrication of a $NiS_2/MoS_2$ hetero-nanosheet modified double-layer HCS material with excellent HER activity.[65] To preserve the nanosheet morphology, Luan *et al.* assembled the $Ni(OH)_2$ nanosheets first onto DLHCs *via* hydrolysis of the nickel salts. The subsequent sulfurization of these $Ni(OH)_2$ nanosheets occurred concurrently with $MoS_2$ formation, leading to the *in situ* generation of $NiS_2/MoS_2$ composite nanosheets, with the resulting DLHCs@$NiS_2/MoS_2$ heterostructures (Fig. 12) exhibiting outstanding HER performance across a wide pH range.[65] Based on the TEM data (Fig. 12a–c) collected for the DLHCs@$NiS_2/MoS_2$ heterostructures synthesized using optimized parameters (DLHCs@$NiS_2/MoS_2$-6), the average spacing between the dual spherical carbon shells is approximately 15 nm. As shown in Fig. 12c, the formation of $NiS_2/MoS_2$ heterojunctions was evident with quite large ultrathin $NiS_2/MoS_2$ nanosheets uniformly coated onto the surfaces of the DLHCs. The measured interlayer spacing of 0.65 nm corresponded to the (002) plane of 2H-$MoS_2$, and the lattice fringes with a spacing of 0.25 nm were assigned to the (210) plane of $NiS_2$.[65,110] The outer carbon shell exhibiting uniformly distributed mesopores was crucial for providing abundant nucleation sites for heterojunction growth, with a well controlled efficient growth process leading to homogeneous distribution of $NiS_2$ and $MoS_2$ on the DLHC base.

Similar to other $MoS_2$ involved catalyst systems, the HER pathway of this DLHCs@$NiS_2/MoS_2$ composite reported by Luan *et al.* primarily followed the Volmer–Tafel and Volmer–Heyrovsky mechanisms.[13,64,65] As shown in the LSV curves in Fig. 12d, the DLHCs@$NiS_2/MoS_2$ electrode exhibited the lowest overpotential among all the tested composite systems. The corresponding Tafel slopes (Fig. 12e) increased with higher $MoS_2$ loading, accompanied by a decline in HER activity, demonstrating that the incorporation of $NiS_2$ played the key role in enhancing the catalytic performance of the composite system. This improvement was attributed to the increased number of exposed active sites introduced by the $NiS_2$ components. Moreover, the S-edge sites of $MoS_2$ nanosheets served as the primary catalytic centres for HER, and excessive $MoS_2$ loading led to nanosheet agglomeration, thereby reducing their accessibility. The formation of a well-defined heterojunction between $MoS_2$ and $NiS_2$ also modulated the electronic structure, facilitated charge transport and promoted more efficient

 

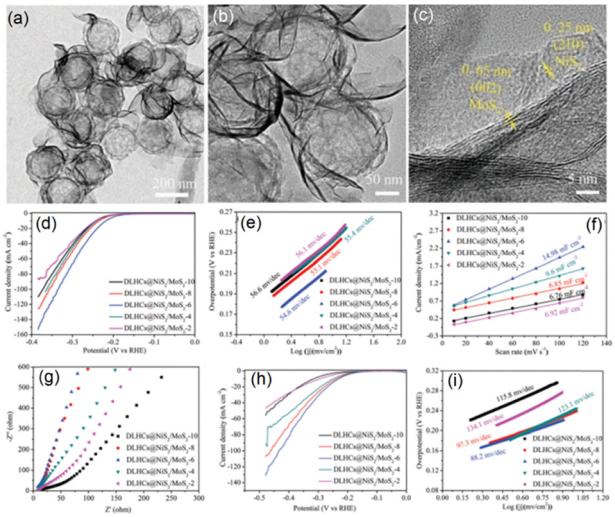

Fig. 12 (a)–(c) TEM images of the DLHCs@$NiS_2$/$MoS_2$-6 composites. (d) HER polarization curves of the samples measured in 0.5 M $H_2SO_4$. (e) Corresponding Tafel plots derived from panel (d). (f) Double-layer capacitance ($C_{dl}$) values of the samples. (g) Electrochemical impedance spectra. (h) HER polarization curves obtained in 1 M KOH. (i) Corresponding Tafel plots derived from panel (h). Reproduced with permission from ref. 65. Copyright 2022 Wiley-VCH GmbH.

water dissociation of the material, collectively contributing to the observed superior HER activity of the composite system.[65]

The reaction kinetics at the electrode–electrolyte interface during the HER were further examined by Luan *et al.*[65] The EIS spectra shown in Fig. 12g indicate that the DLHCs@$NiS_2$/$MoS_2$-6 composites exhibited the steepest slope in the low-frequency region, reflecting its superior electrochemical kinetics for the HER. The catalytic performance in alkaline media is presented in Fig. 12h and i. The DLHCs@$NiS_2$/$MoS_2$-6 system with optimized parameters showed the lowest onset potential (139 mV at 1 mA $cm^{-2}$) and the smallest overpotential (230 mV at 10 mA $cm^{-2}$). As the $MoS_2$ loading increased, the Tafel slope decreased from 134.1 mV $dec^{-1}$ (DLHCs@$NiS_2$/$MoS_2$-2) to 88.2 mV $dec^{-1}$ (DLHCs@$NiS_2$/$MoS_2$-6), suggesting a shift in the rate-determining step from the Volmer step to the Heyrovsky step.[65] However, excessive $MoS_2$ loading led to performance deterioration, likely due to nanosheet agglomeration and reduced accessibility to active sites.

## Ni and Co sulphides on HCSs as catalysts

Except for the $MoS_2$ involved composite systems, a variety of Ni and Co sulfide components have also been directly employed to modify HCSs due to their excellent electrochemical properties, for instance, Ni sulphides exhibiting outstanding $H_2$ generation activity and structural motifs that resemble the active centres of hydrogenase enzymes.[111] Various Ni sulfide phases, including NiS, $NiS_2$, $Ni_3S_2$, $Ni_3S_4$, and $Ni_7S_6$, have therefore emerged as promising electrocatalyst options for energy storage/conversion applications, especially when integrated with HCS substrates. Reddy *et al.* synthesized a core–shell HCS@nickel–sulfide nanocomposite that achieved a high specific capacitance of 1022 F $g^{-1}$ at 1 A $g^{-1}$.[112] Recently, Liu and co-workers reported Ni sulfide composites supported on DLHCs for the HER, achieving a quite low onset overpotential of 162 mV, a Tafel slope of 88.23 mV $dec^{-1}$, and a high specific capacitance of 1160 F $g^{-1}$ at 1 A $g^{-1}$ (Fig. 13, constructed using sol–gel-derived $SiO_2$ templates, with the synthetic route illustrated in Fig. 13a).[36] Furthermore, an asymmetric supercapacitor device was assembled by Liu *et al.* using DLHCs@NiS/$Ni_3S_4$ as the positive electrode and activated carbon as the negative electrode. This device delivered a specific capacitance of 306 F $g^{-1}$ at 1 A $g^{-1}$ and retained 78.4% of its capacitance when the current density increased to 10 A $g^{-1}$, demonstrating excellent rate capabilities.[36]

According to Liu *et al.*, the Ni sulfide components were deposited onto a double-layer HCS through hydrothermal reaction, producing a uniform and tightly adhered NiS/$Ni_3S_4$ coating, as shown in the TEM images in Fig. 13b–f.[36] The

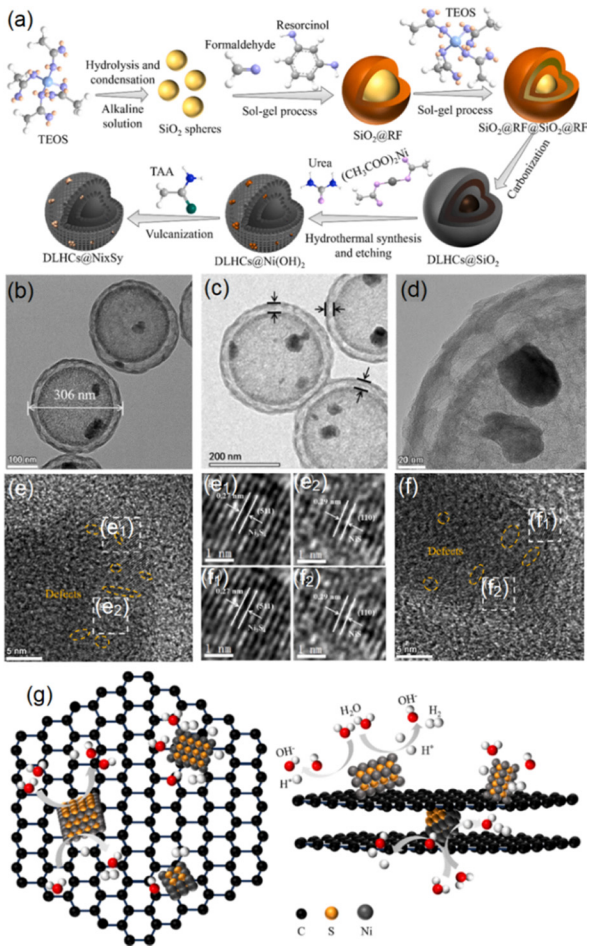

Fig. 13 Synthetic procedures (a) and TEM data at different magnifications (b)–(f) of the DLHCs@$Ni_xS_y$-1 : 2 composite system: ($e_1$) and ($e_2$) enlarged areas circled in (e); ($f_1$) and ($f_2$) enlarged areas circled in (f); with orange dotted lines showing the structural defects. (g) HER mechanism proposed for the DLHCs@$Ni_xS_y$ system in an alkaline environment. Reproduced with permission from ref. 36. Copyright 2024 Elsevier.

further introduction of $SiO_2$ precursors was essential for generating the characteristic double-layer carbon shells. During the following alkaline treatment, the $SiO_2$ was etched away with $Ni(OH)_2$ simultaneously deposited onto the carbon framework. This process preserved the mechanically robust double-layer hollow carbon structures, which functioned both as a conductive backbone and as a stable platform for anchoring the active Ni sulfide phases. High-resolution TEM images (Fig. 13e and f) show clear lattice spacings of 0.39 nm and 0.27 nm, corresponding to the (202) plane of NiS and the (511) plane of $Ni_3S_4$, with the clear boundary between these two sets of lattice fringes confirming the formation of the $NiS/Ni_3S_4$ heterointerfaces. As schematically illustrated in Fig. 13g, in this system, the highly conductive carbon shells acted as an efficient platform for anchoring $Ni_xS_y$ species and enabled rapid electron transport from the graphitic carbon framework to the catalytic Ni sulfide domains where $H_2$ generation took place. Previous studies have also demonstrated that Ni-based active sites can accelerate the initial water dissociation step while assisting in the subsequent removal of $OH^-$ species, improving the overall reaction kinetics.[36,113,114] This DLHCs@$NiS/Ni_3S_4$ material were also used by Liu and co-workers for constructing an asymmetric supercapacitor that could deliver an energy density of 40 Wh $kg^{-1}$ at a power density of 375 W $kg^{-1}$, exhibiting strong durability in both the HER and supercapacitor testing.[36]

In addition, Ni–Co mixed sulfides have also emerged as a promising class of high-performance electrocatalysts, benefiting from the intrinsic catalytic activity of both Ni and Co. Since the HER and OER often require different active site environments and reaction pathways, the target composite catalysts must be tailored to exhibit distinct selectivity for each process.[115,116] Besides, achieving exceptionally high performance with non-noble metal components remains challenging, largely due to interfacial limitations within nanosheets, nanotubes, and nanoneedles, each of which composite structures. Careful control over morphology and the deliberate design of nanostructured catalysts are thus essential strategies for improving catalytic behavior.[117,118] In general, Ni–Co sulfides can be synthesized in various morphologies with significantly different catalytic responses. A recent example involved the growth of Ni–Co sulfides on a DLHC substrate, constructing $NiCo_2S_4$@DC composites using a hydrothermal method.[96] The resulting $NiCo_2S_4$ hollow spherical tube structures contained internal cavities that helped buffer mechanical stress from volume changes during operation, while their high surface area increased the interfacial contact between the electrolyte and the active materials, facilitating efficient charge transport and enhancing catalytic performance.

Fig. 14a outlines the detailed synthetic strategy used to construct a Ni–Co mixed sulphide incorporated hybrid catalyst ($NiCo_2S_4$@DCs, with $NiCo_2S_4$ directly grown onto hollow double-layered carbon nanospheres (DCs)) developed by Yang's group.[96] In this approach, the sol–gel-derived $SiO_2$ spheres acted as the sacrificial templates.[96] A resorcinol-formaldehyde polymer layer was deposited onto the $SiO_2$ cores ($SiO_2$@RF), followed by coating, carbonization, and template removal steps

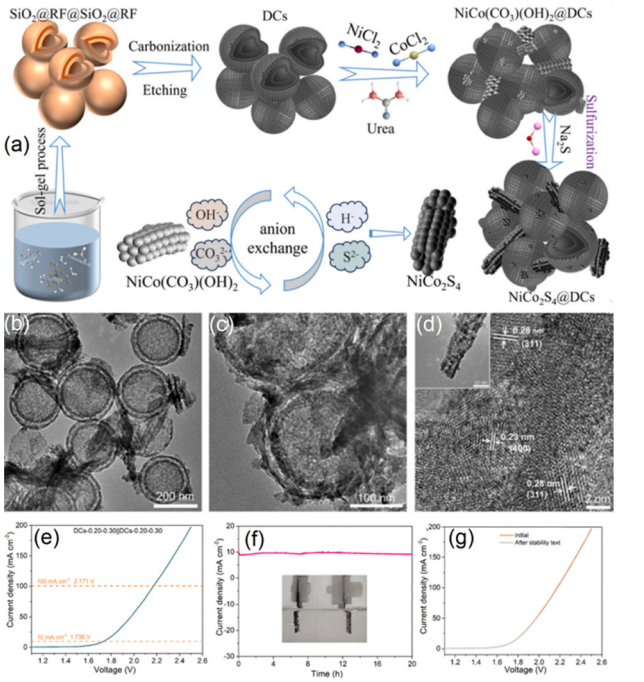


Fig. 14 (a) Schematic illustration of the synthesis of $NiCo_2S_4$@DCs. (b)–(d) TEM data of the composite system. (e) LSV curve of the composites recorded in 1 M KOH. (f) Chronoamperometry measurement at 1.736 V for 20 h in 1 M KOH; the inset depicts the two-electrode operating configuration. (g) LSV data collected before/after the chronoamperometry test. Reproduced with permission from ref. 96. Copyright 2024 Elsevier.

to fabricate the DLHC base. Moreover, $NiCo(CO_3)(OH)_2$ was deposited onto the carbon spheres and converted into the $NiCo_2S_4$ phase through reaction with sulfide ions achieving uniform dispersion of $NiCo_2S_4$ components and the formation of well-defined interfaces with the carbon framework. In this case, the hydrothermal treatment was crucial for the nucleation and direct growth of $NiCo_2S_4$ nanotubes onto DLHC surfaces. The TEM images of the constructed $NiCo_2S_4$@DC composites (Fig. 14b–d) demonstrated that the $NiCo_2S_4$ formed porous hollow tubular structures that distributed irregularly around the carbon base. The confined geometry of the HCSs restricted the longitudinal growth of $NiCo_2S_4$ tubes, resulting in their characteristic short tube morphology. The TEM data further confirmed the crystalline nature of this active phase, showing lattice spacings of 0.23 nm and 0.28 nm corresponding to the (400) and (311) planes of $NiCo_2S_4$.[96]

According to Yang *et al.*, the Ni/Co precursor ratios were varied to synthesize a series of composites (DCs-*x*-*y* with *x* and *y* denoting the molar ratios of the Ni and Co precursors). The high performance of the optimized composition (DCs-0.20-0.30) arose from the high surface area and monodisperse HCSs, which promoted uniform $NiCo_2S_4$ distribution, improved electrical conductivity, and increased the number of accessible active sites. The $NiCo_2S_4$@DCs system exhibited reasonably high HER and OER activity in alkaline media and delivered excellent overall water splitting performance with excellent operational stability (for 20 h at 10 mA $cm^{-2}$), requiring only 1.736 V to reach

 

Table 2 HER activity comparison on TMD-decorated hollow carbon nanostructures

| Sample | Overpotential (mV/at 10 mA $cm^{-2}$) | Tafel slope (mV $dec^{-1}$) | Ref. |
|---|---|---|---|
| $MoS_2$@HCSs | 207.0 | 62.0 | 64 |
| $MoS_2$@ HCSs | 162.0 | 44.0 | 119 |
| P-$MoS_2$@N-HCSs | 117.0 | 68.0 | 37 |
| $MoS_2$@DLHCs | 174.4 | 74.7 | 35 |
| $MoS_2$@HCSs | 190.0 | 79.9 | 50 |
| MoSSe@HCSs | 186.0 | 53.2 | 50 |
| $NiS_2/MoS_2$@DLHCs | 139.0 | 54.6 | 65 |
| $NiS/Ni_3S_4$@DLHCs | 162.0 | 88.2 | 36 |
| $NiCo_2S_4$@ DLHCs | 206.0 | 71.0 | 96 |
| Ni-$MoS_2$@CNTs | 158 | 62.3 | 18 |

10 mA $cm^{-2}$ (Fig. 14e–g). The observed HER activity of this composite system in acidic media was superior to that observed in alkaline media, with the catalytic activity of the optimized $NiCo_2S_4$@DC system surpassing that of bare DCs, $NiCo_2S_4$, $Ni_xS_y$@DCs, and $Co_xS_y$@DCs across all tested conditions. These highlight the potential of such Ni–Co sulphide hybrid structures to guide the rational design of electrocatalysts optimized for different electrolyte environments in both $H_2$ generation and overall water splitting. To facilitate a clear comparison of HER performance among the TMD decorated HCSs composites, Table 2 summarizes the overpotentials and Tafel slopes of some selected examples reported in the literature. The electrochemical activity of TMDs is highly sensitive to their synthesis conditions and spatial distribution, both of which critically influence their catalytic behavior.[119]

## Challenges and perspectives

This review has examined strategies for controlling the growth of TMDs on HCSs to develop high-performance catalysts for sustainable energy storage and conversion, with particular emphasis on applications in water splitting and supercapacitors. We first summarized advances in HCS engineering, including hard-template synthesis, shell-thickness modulation, and non-metal heteroatom doping that enable precise structural control. The subsequent sections discussed the integration of $MoS_2$ nanosheets with HCSs, followed by an analysis of how Se, Ni, and Co incorporation modifies the catalytic behaviour of $MoS_2$/HCSs composites. Beyond $MoS_2$ and $MoSe_2$ systems, recent progress on Ni- and Co-sulfide/HCS hybrids was also highlighted, with attention to their catalytic performance and structural advantages. Throughout the review, we emphasized synthesis kinetics, heterostructure formation, and interfacial characteristics, all of which play critical roles in determining catalytic activity. Despite the substantial number of studies published on TMD/HCS composites, significant challenges remain. The pronounced differences in structure, bonding, and physicochemical properties between TMDs and carbon-based hosts mean that both fundamental understanding and practical implementation are still developing. Key research directions and remaining challenges for advancing these composite catalysts are outlined below.

(i) Precise control over the shell thickness and structure of HCSs remains a long-standing challenge. Although hard template methods have been employed for decades, the template removal step is still hard to regulate with precision, often leading to variability in shell thickness. Residual template or precursor species can negatively influence catalytic performance and hinder scalability. Non-metal doping has been explored to introduce additional active sites, yet achieving uniform incorporation of dopant atoms throughout the carbon framework remains difficult. These limitations highlight the need for new synthetic strategies capable of delivering precise structural control, homogeneous doping, and improved catalytic activity.

(ii) TMD modified catalysts exhibit diverse crystal structures and bonding environments, making composite formation inherently complex. The formation of TMD composites often requires multistep or delicate synthesis routes, and further progress will depend on design strategies grounded in solid theoretical understanding. Because TMDs can form alloys, composite phases, homojunctions, and heterostructures, the spatial arrangement and interaction of each component strongly influence the final catalytic behavior. Progress in new synthetic methodologies, computational modelling, mechanism study, and advanced in-situ characterization will be essential for establishing clear structure–property relationships and guiding the rational design of next-generation TMDs incorporated catalysts.

(iii) Interface engineering remains a central but underdeveloped frontier. Interface engineering represents a crucial avenue for constructing TMD-based heterostructures and achieving high catalytic efficiency. For example, $MoS_2/MoSe_2$ heterostructures supported on HCSs involve multiple interfacial interactions, between $MoS_2$ and $MoSe_2$, between each TMD and the HCS hosts, and across the combined junctions. The quality and continuity of these interfaces largely determine the resulting catalytic performance of the material. Redox behavior, band gap alignment, and charge carrier transport within the composite system are all strongly governed by interfacial characteristics. Consequently, deeper investigation into interface formation, optimization, and stabilization is essential for advancing the TMD-HCS hybrid systems.

(iv) Long-term operational stability of *e.g.*, HER and OER processes remains a central concern, as maintaining catalytic integrity under harsh electrochemical conditions is essential for real world water splitting and energy storage applications. Although the porous nanostructures of TMD-HCSs effectively immobilizes TMDs and mitigates aggregation or corrosion, further optimization is required to ensure consistent performance over extended cycling. Another challenge lies in maximizing interfacial electronic coupling. While current designs enhance active site exposure and charge transport pathways, the overall spatial utilization within the composite structure is still not fully exploited. Achieving more efficient electron/ion transport networks will be crucial for advancing both water

splitting and supercapacitor technologies.[120,121] Looking forward, the development of next-generation TMD–HCS nanostructures would depend on the strategic incorporation of new functional components. Improving energy conversion efficiency, particularly under practical operating conditions, remains a key objective. Emerging concepts, such as photothermal-responsive electrocatalysts engineered through porogen-mediated structural design, offer promising directions, with these dual-function systems integrating photothermal conversion with electrocatalysis, enabling broad spectrum light harvesting and significantly enhanced electrochemical activity. Future research could focus on *e.g.*, refining structural stability, deepening interfacial coupling, and exploring multifunctional structures capable of leveraging external stimuli. Such advances will be essential for translating TMD-HCSs composites from laboratory demonstrations into scalable, high-performance energy conversion technologies.

## Author contributions

Xiao Zhang: conceptualization, data curation, formal analysis, investigation, methodology, writing – original draft, funding acquisition, project administration, and writing – review & editing.

## Conflicts of interest

There are no conflicts to declare.

## Data availability

No primary research results, software or code have been included and no new data were generated or analysed as part of this review.

## Acknowledgements

This work was partly supported by JSPS KAKENHI Grant Number JP25K23518.

## Notes and references

1 X. Zhang and P. Yang, *Phys. Chem. Chem. Phys.*, 2025, **27**, 25254–25265.
2 W. Yan, Y. Mou, M. Li, K. Ma, Z. Xu, T. Lu, H. Du, C. Wang, H. Sun, L. Chen, Y. Tang, Y. Wang and G. Fu, *Adv. Mater.*, 2025, **37**, 2506936.
3 X. R. Zhang, Y. Lyu, J. Ding, X. Wang, B. Johannessen, S. P. Jiang and J. Zheng, *Sci. Adv.*, 2025, **11**, eadr8651.
4 X. Zhang, X. Xia and P. Yang, *Environ. Sci.: Nano*, 2024, **11**, 4186–4195.
5 X. Zhang, X. Ji and P. Yang, *Appl. Surf. Sci.*, 2026, **723**, 165666.
6 X. Wang, J. Hu, T. Lu, H. Wang, D. Sun, Y. Tang, H. Li and G. Fu, *Angew. Chem., Int. Ed.*, 2025, **64**, e202415306.
7 Q. Liu, Y. Sun, Y. Xie, F. Yao, X. Gao, H. Bai, K. Zhang, R. Liu and H. Yue, *J. Power Sources*, 2024, **605**, 234537.
8 X. R. Zhang, Y. Lyu, C. Chen, J. Zheng, S. P. Jiang and S. Wang, *Proc. Natl. Acad. Sci. U. S. A.*, 2024, **121**, e2311326121.
9 X. Zhang and P. Yang, *Langmuir*, 2025, **41**, 7191–7211.
10 C. Wang, X. Zhang, Y. Zhu, K. Zhu, X. Luan and P. Yang, *Electrochim. Acta*, 2023, **454**, 142386.
11 S. Huang, D. Ma, S. Zhai, K. Chen, W. Lai, W. Xiao, H. Liu, Z. Su, J. Zeng and Y. Tong, *J. Power Sources*, 2024, **598**, 234195.
12 X. Zhang, X. Zhang, P. Yang and S. P. Jiang, *J. Electroanal. Chem.*, 2021, **895**, 115510.
13 X. Zhang, P. Yang and S. P. Jiang, *Carbon*, 2021, **175**, 176–186.
14 X. Wang, M. Li, Y. Tang, H. Li and G. Fu, *Prog. Mater. Sci.*, 2026, **155**, 101539.
15 H. Lv, S. Wang, Z. Xiao, C. Qin, S. Zhai, G. Wang, Z. Zhao and Q. An, *J. Power Sources*, 2021, **493**, 229679.
16 J. Chen, Y. Guo, Y. Wen, L. Huang, Y. Xue, D. Geng, B. Wu, B. Luo, G. Yu and Y. Liu, *Adv. Mater.*, 2013, **25**, 992–997.
17 Y. Liu, X.-Y. Yu, Y. Fang, X. Zhu, J. Bao, X. Zhou and X. W. Lou, *Joule*, 2018, **2**, 725–735.
18 T. Dong, X. Zhang, P. Wang, H. S. Chen and P. Yang, *Electrochim. Acta*, 2020, **338**, 135885.
19 X. Zhang, P. Yang and S. P. Jiang, *Int. J. Hydrogen Energy*, 2021, **46**, 2065–2074.
20 Q. Shen, Z. Jiang, X. Tian, H. Zhu and Z. J. Jiang, *J. Alloys Compd.*, 2021, **884**, 161073.
21 F. Yang, W. Qiao, L. Yu, S. Wang and L. Feng, *Chem. Eng. J.*, 2024, **483**, 149055.
22 Z. J. Jiang, G. Xie, B. Deng and Z. Jiang, *Electrochim. Acta*, 2018, **285**, 103–110.
23 Y. Kuang, W. Qiao, F. Yang and L. Feng, *J. Energy Chem.*, 2023, **85**, 447–454.
24 W. Chen, R. Qiao, C. Song, L. Zhao, Z. J. Jiang, T. Maiyalagan and Z. Jiang, *J. Catal.*, 2020, **381**, 363–373.
25 J. Q. Chi, W. K. Gao, J. H. Lin, B. Dong, K. L. Yan, J. F. Qin, B. Liu, Y. M. Chai and C. G. Liu, *Catal. Today*, 2019, **330**, 259–267.
26 X. Zhang and P. Yang, *Int. J. Miner., Metall. Mater.*, 2024, **31**, 2368–2389.
27 G. Ghanashyam and H. Kim, *J. Power Sources*, 2024, **596**, 234088.
28 T. Wang, X. Zhang, P. Yang and S. P. Jiang, *Inorg. Chem. Front.*, 2020, **7**, 3578–3587.
29 T. Dong, X. Zhang, P. Wang, H. S. Chen and P. Yang, *Carbon*, 2019, **149**, 222–233.
30 T. Dong, X. Zhang, Y. Cao, H. S. Chen and P. Yang, *Inorg. Chem. Front.*, 2019, **6**, 1073–1080.
31 Y. Zhang, X. Zong, L. Zhan, X. Yu, J. Gao, C. Xun, P. Li and Y. Wang, *Electrochim. Acta*, 2018, **284**, 89–97.
32 L. Yu, X. He, L. Tang, X. Wang, W. Cai, Y. He, Y. Sun, G. Zhu, J. Rosen and H. Jin, *J. Power Sources*, 2025, **641**, 236852.
33 X. Wei, X. Li, C. Lv, X. Mo and K. Li, *Electrochim. Acta*, 2020, **354**, 136590.
34 H. Liao, H. Zhang, H. Hong, Z. Li and Y. Lin, *Electrochim. Acta*, 2017, **257**, 210–216.
35 X. Luan, K. Zhu, X. Zhang and P. Yang, *Electrochim. Acta*, 2022, **407**, 139929.
36 C. Liu, X. Zhang, Y. Cheng, X. Hao and P. Yang, *Electrochim. Acta*, 2024, **477**, 143751.
37 Y. Wei, X. Zhang, Z. Zhao, H. S. Chen, K. Matras-Postolek, B. Wang and P. Yang, *Electrochim. Acta*, 2019, **297**, 553–563.
38 Z. Chen, R. Cao, Y. Ge, Y. Tu, Y. Xia and X. Yang, *J. Power Sources*, 2017, **363**, 356–364.
39 Y. Sun, Y. Shi, X. Zhang, F. Cao, L. Huang and Y. Chen, *Carbon*, 2025, **240**, 120352.
40 W. Shi, X. Zhang, Y. Tian and P. Yang, *J. Environ. Chem. Eng.*, 2024, **12**, 114018.
41 S. Wang, X. Zhang, C. Li, Y. Tian and P. Yang, *Int. J. Hydrogen Energy*, 2024, **90**, 853–864.
42 C. Wang, X. Wu, H. Sun, Z. Xu, C. Xu, X. Wang, M. Li, Y. Wang, Y. Tang, J. Jiang, K. Sun and G. Fu, *Energy Environ. Sci.*, 2025, **18**, 4276–4287.
43 Y. Ma, S. Luo, M. Tian, J. E. Lu, Y. Peng, C. Desmond, Q. Liu, Q. Li, Y. Min, Q. Xu and S. Chen, *J. Power Sources*, 2020, **450**, 227659.
44 S. Tong, X. Zhang and P. Yang, *Environ. Res.*, 2023, **236**, 116805.
45 C. Li, X. Zhang, T. Song, Y. Tian, S. Wang and P. Yang, *J. Environ. Chem. Eng.*, 2024, **12**, 113396.
46 Y. Chen, G. Meng, T. Yang, C. Chen, Z. Chang, F. Kong, H. Tian, X. Cui, X. Hou and J. Shi, *J. Chem. Eng.*, 2022, **450**, 138157.
47 H. Shi, Y. Zhang, N. Pang, S. Xu, D. Xiong, L. Wang, P. Yang and P. K. Chu, *Electrochem. Acta*, 2023, **439**, 141596.

 

48 C. Li, Y. Tian, S. Wang, P. Yang and X. Zhang, *J. Environ. Chem. Eng.*, 2024, **12**, 114170.
49 X. Zhang, K. Zhu, C. Xie and P. Yang, *Carbon*, 2024, **220**, 118884.
50 X. Luan, K. Zhu, X. Zhang and P. Yang, *Langmuir*, 2021, **37**(27), 8314–8322.
51 J. Zhang, W. Xi, P. Du, Z. Xie, Y. Zhang, R. Wang, B. He, Y. Gong, H. Wang and J. Jin, *Electrochim. Acta*, 2023, **471**, 143385.
52 X. Li, S. Bai, Z. Zhu, J. Sun, X. Jin, X. Wu and J. Liu, *Langmuir*, 2017, **33**, 1248–1255.
53 L. Wang, L. Rao, B. Xia, L. Wang, L. Yue, Y. Liang and X. Hu, *Carbon*, 2018, **130**, 31–40.
54 D. Bin, Z. Chi, Y. Li, K. Zhang, X. Yang, Y. G. Sun and L. Wan, *J. Am. Chem. Soc.*, 2017, **139**, 13492–13498.
55 D. Zhu, Y. Wang, X. Yang, H. Wang, Y. Xu, Z. Wang, Y. Tian and H. Lu, *Electrochim. Acta*, 2025, **542**, 147427.
56 J. Du, Y. Zhang, H. Wu, S. Hou and A. Chen, *Carbon*, 2020, **156**, 523–528.
57 D. Khalafallah, X. Quan, C. Ouyang, M. Zhi and Z. Hong, *Renew. Energy*, 2021, **170**, 60–71.
58 J. Du, S. Zong, Y. Zhang, S. Hou and A. Chen, *J. Colloid. Interface Sci.*, 2020, **565**, 245–253.
59 L. Zhou, Z. Zhuang, H. Zhao, M. Lin, D. Zhao and L. Mai, *Adv. Mater.*, 2017, **29**, 1602914.
60 A. Fu, C. Wang, F. Pei, J. Cui, X. Fang and N. Zheng, *Small*, 2019, **15**, 1804786.
61 H. Tian, J. Liang and J. Liu, *Adv. Mater.*, 2019, **31**, 1903886.
62 D. P. Li, Y. C. Sun, X. Wang, S. Wu, S. C. Han and Y. Yang, *RSC Adv.*, 2017, **7**, 37983–37989.
63 L. L. Han, W. W. Wu, C. Yuan, Z. Wang, X. B. Zhou, X. M. Chen and P. Liu, *J. Mater. Chem. C*, 2023, **11**, 5534–5545.
64 C. Liu, P. Yang and X. Zhang, *Int. J. Hydrogen Energy*, 2025, **97**, 1348–1356.
65 X. Luan, K. Zhu, C. Wang, W. Shi, A. Szymska, K. Matras-Postolek and P. Yang, *Adv. Mater. Interfaces*, 2022, 2201661.
66 H. Zhang, B. Wang, A. Feng, N. Zhang, Z. Jia, Z. Huang, X. Liu and G. Wu, *Composites, Part B*, 2019, **167**, 690–699.
67 X. Wang, J. I. Feng, Y. Bai, Q. Zhang and Y. Yin, *Chem. Rev.*, 2016, **116**, 10983.
68 Z. Li, D. Wu, Y. Liang, R. Fu and K. Matyjaszewski, *J. Am. Chem. Soc.*, 2014, **136**, 4805–4808.
69 S. Tanaka, H. Nakao, T. Mukai, Y. Katayama and Y. Miyake, *J. Phys. Chem. C*, 2012, **116**, 26791–26799.
70 X. L. Fang, J. Zang, X. L. Wang, M. S. Zheng and N. F. Zheng, *J. Mater. Chem. A*, 2014, **2**, 6191–6197.
71 M. Sevilla, P. Valle-Vigon and A. B. Fuertes, *Adv. Funct. Mater.*, 2011, **21**, 2781–2787.
72 K. Wang, L. Huang, S. Razzaque, S. Jin and B. Tan, *Small*, 2016, **23**, 3134–3142.
73 C. Q. Yuan, X. H. Liu, M. Y. Jia, Z. X. Luo and J. N. Yao, *J. Mater. Chem. A*, 2015, **3**, 3409–3415.
74 X. L. Fang, J. Zang, X. L. Wang, M. S. Zheng and N. F. Zheng, *J. Mater. Chem. A*, 2014, **2**, 6191–6197.
75 Y. H. Dai, H. Jiang, Y. J. Hu, Y. Fu and C. Z. Li, *Ind. Eng. Chem. Res.*, 2014, **53**, 3125–3130.
76 J. Wang, L. F. Shen, B. Ding, P. Nie, H. F. Deng, H. Dou and X. G. Zhang, *RSC Adv.*, 2014, **4**, 7538–7544.
77 Q. G. Shao, J. Tang, Y. X. Lin, F. F. Zhang, J. S. Yuan, H. Zhang, N. Shinya and L. C. Qin, *J. Mater. Chem. A*, 2013, **1**, 15423–15428.
78 J. P. Han, G. Y. Xu, B. Ding, J. Pan, H. Dou and D. R. MacFarlane, *J. Mater. Chem. A*, 2014, **2**, 5352–5357.
79 M. C. Hsiao, C. Y. Chang, L. J. Niu, F. Bai, L. J. Li, H. H. Shen, J. Y. Lin and T. W. Lin, *J. Power Sources*, 2017, **345**, 156–164.
80 J. Liu, Y. Pan, L. Yu, Z. Gao, S. Zhang, D. Lan, Z. Jia and G. Wu, *Carbon*, 2025, **238**, 120233.
81 X. Xu, W. Zhong, M. Chen, L. Zhang, G. Liu and Y. Du, *Int. J. Hydrogen Energy*, 2021, **46**, 8567–8577.
82 D. C. Nguyen, T. L. L. Doan, S. Prabhakaran, D. T. Tran, D. H. Kim, J. H. Lee and N. H. Kim, *Nano Energy*, 2021, **82**, 105750.
83 S. Gao, S. Chen, F. Shi, W. Jiang and J. Chen, *J. Power Sources*, 2024, **591**, 233866.
84 J. Cheon, J. E. Gozum and G. S. Girolami, *Chem. Mater.*, 1997, **9**, 1847–1853.
85 Q. Li, J. T. Newberg, E. C. Walter, J. C. Hemminger and R. M. Penner, *Nano Lett.*, 2004, **4**, 277–281.
86 Y. Tian, X. Zhao, L. Shen, F. Meng, L. Tang, Y. Deng and Z. Wang, *Mater. Lett.*, 2006, **60**, 527–529.
87 S. J. Lee, Y. S. Son, J. H. Choi, S. S. Kim and S. Y. Park, *Catalysts*, 2021, **11**, 1229.
88 F. Yang, H. Huang, J. Zhu, W. Dong, Q. Wu and H. Li, *J. Mater. Sci.: Mater. Electron.*, 2022, **33**, 21677–21687.
89 Y. Zhang, T. He, G. Liu, L. Zu and J. Yang, *Nanoscale*, 2017, **9**, 10059–10066.
90 S. G. Mohamed, I. Hussain and J. J. Shim, *Nanoscale*, 2018, **10**, 6620–6628.
91 S. J. Lee, Y. S. Son, J. H. Choi, S. S. Kim and S. Y. Park, *Catalysts*, 2021, **11**, 1229.
92 W. Li, X. Xu, Y. Yang, Y. Huang, J. Jiang, W. Liu, M. Jing, Y. Bai, Y. Yang, T. Wu and X. Wang, *J. Alloys Compd.*, 2023, **934**, 167838.
93 X. Zhang, P. Yang and S. P. Jiang, *J. Power Sources*, 2021, **510**, 230420.
94 J. Li, A. Listwan, J. Liang, F. Shi, K. Li and J. Jia, *J. Chem. Eng.*, 2022, **422**, 130100.
95 K. Nie, N. Li, B. Li, Y. Yuan, Y. Zhang, P. Liu, S. Chong, J. Hu, Z. Liu and W. Huang, *J. Chem. Eng.*, 2023, **475**, 146066.
96 C. Liu, X. Zhang, X. Hao and P. Yang, *J. Alloys Compd.*, 2024, **1002**, 175110.
97 L. Ye, S. Chen, W. Li, M. Pi, T. Wu and D. Zhang, *J. Phys. Chem. C*, 2015, **119**, 9560–9567.
98 H. Li, Q. Zhang, C. C. R. Yap, B. K. Tay, T. H. T. Edwin, A. Olivier and D. Baillargeat, *Adv. Funct. Mater.*, 2012, **22**, 1385–1390.
99 Y. Yang, X. Liu, Z. Zhu, Y. Zhong, Y. Bando, D. Golberg, J. N. Yao and X. Wang, *Joule*, 2018, **2**, 1075–1094.
100 Y. Zhang, L. Zuo, Y. Huang, L. Zhang, F. Lai and W. Fan, *ACS Sustain. Chem. Eng.*, 2015, **3**, 3140–3148.
101 Y. Zhang, L. Zhang, B. Zhou, H. Cheng, Q. Zhang and B. Zhang, *Carbon*, 2023, **205**, 562–572.
102 C. Liu, K. Wang, X. Zheng, X. Liu, Q. Liang and Z. Chen, *Carbon*, 2018, **139**, 1–9.
103 X. Fu, Q. Zheng, L. Li and M. Cao, *Carbon*, 2022, **197**, 324–333.
104 F. Zheng, W. Zhong, Q. Deng, Q. Pan, X. Ou, Y. Liu, X. Xiong, C. Yang, Y. Chen and M. Liu, *Chem. Eng. J.*, 2019, **357**, 226–236.
105 G. Liu, Q. Zeng, X. Sui, S. Tian, X. Sun, Q. Wu, X. Li, Y. Zhang, K. Tao, E. Xie and Z. Zhang, *Small*, 2023, **19**, 2301085.
106 D. Tian, X. Song, Y. Qiu, X. Sun, B. Jiang, C. Zhao, Y. Zhang, X. Xu, L. Fan and N. Zhang, *ACS Nano*, 2021, **15**, 16515–16524.
107 G. Zhao and H. Zhu, *Adv. Mater.*, 2020, **32**, 1905756–1905777.
108 Z. Akbar Mohammadi, B. Ameri and S. Saeed Hossein Davarani, *Chem. Eng. J.*, 2023, **470**, 144132.
109 T. Wang, J. Lei, Y. Wang, L. Pang, F. Pan, K. J. Chen and H. Wang, *Small*, 2022, **18**, 2203307.
110 J. Hu, C. Zhang, P. Yang, J. Xiao, T. Deng, Z. Liu, B. Huang, M. K. H. Leung and S. Yang, *Adv. Funct. Mater.*, 2020, **30**, 1908520.
111 H. Wang, W. Zhang, X. Zhang, S. Hu, Z. Zhang, W. Zhou and H. Liu, *Nano Res.*, 2021, **14**, 4857–4864.
112 A. S. Justin, P. Vickramman and B. J. Reddy, *Curr. Appl. Phys.*, 2018, **19**, 295–302.
113 T. Chen, Z. Liu, Z. Liu, X. Tao, H. Fan and L. Guo, *Mater. Lett.*, 2019, **248**, 1–4.
114 J. Deng, Q. Gong, H. Ye, K. Feng, J. Zhou, C. Zha, J. Wu, J. Chen, J. Zhong and Y. Li, *ACS Nano*, 2018, **12**, 1829–1836.
115 H. Chen, L. Yang, R. Wang, W. Zhang, R. Liu, Y. Yun, N. Wang, S. Ramakrishna, L. Jiao and Y. Long, *Small*, 2023, **19**, 2304086.
116 S. Chen, H. Chen, M. Fan, C. Li and K. Shu, *J. Sol–Gel Sci. Technol.*, 2016, **80**, 119–125.
117 Z. Ji, L. Chen, K. Liu, D. Ma, S. Zhang, G. Zhu, X. Shen, P. Song and S. Premlatha, *Appl. Surf. Sci.*, 2022, **574**, 15172.
118 J. Cheng, L. Lin, W. Hong, L. Lin, H. Chen and H. Lai, *Electrochim. Acta*, 2018, **283**, 1245–1252.
119 W. W. Liu, M. H. Zhu and J. H. Liu, *Inorg. Chem. Front.*, 2018, **5**(9), 2198–2204.
120 T. Yang, Q. Pang, G. Yang, R. Wang, J. Dang, H. Yang, Z. Wang, R. Feng, A. Arshad, X. Xu and S. Yun, *Carbon*, 2026, **246**, 120858.
121 F. Liu, G. Li, H. Li, C. Hu, P. F. Msomi, H. Guo and Y. Liu, *Carbon*, 2025, **244**, 120659.